J. Fluid Mech. (2024), *vol*. 1000, A9, doi:10.1017/jfm.2024.991

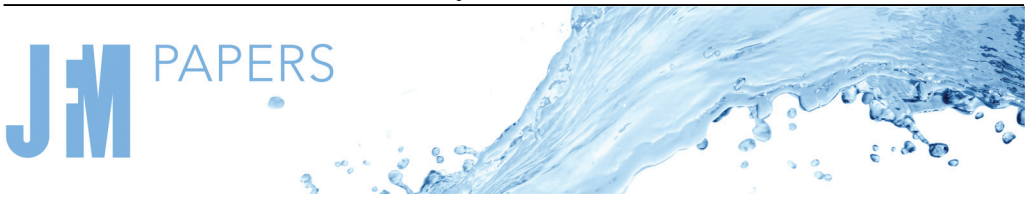

Instability evolution on a shock-accelerated cylindrical fluid layer with arbitrary Atwood numbers

Ming Yuan[1], **Zhiye Zhao**[1,2,†], **Luoqin Liu**[1,†], **Pei Wang**[3], **Nan-Sheng Liu**[1] and **Xi-Yun Lu**[1]

[1]Department of Modern Mechanics, University of Science and Technology of China, Hefei, Anhui 230026, PR China

[2]Department of Mechanical and Aerospace Engineering, The Hong Kong University of Science and Technology, Hong Kong, PR China

[3]Institute of Applied Physics and Computational Mathematics, Beijing 100094, PR China

(Received 3 March 2024; revised 19 September 2024; accepted 7 October 2024)

Developing a model to describe the shock-accelerated cylindrical fluid layer with arbitrary Atwood numbers is essential for uncovering the effect of Atwood numbers on the perturbation growth. The recent model (*J. Fluid Mech.*, vol. 969, 2023, p. A6) reveals several contributions to the instability evolution of a shock-accelerated cylindrical fluid layer but its applicability is limited to cases with an absolute value of Atwood numbers close to 1, due to the employment of the thin-shell correction and interface coupling effect of the fluid layer in vacuum. By employing the linear stability analysis on a cylindrical fluid layer in which two interfaces separate three arbitrary-density fluids, the present work generalizes the thin-shell correction and interface coupling effect, and thus, extends the recent model to cases with arbitrary Atwood numbers. The accuracy of this extended model in describing the instability evolution of the shock-accelerated fluid layer before reshock is confirmed via direct numerical simulations. In the verification simulations, three fluid-layer configurations are considered, where the outer and intermediate fluids remain fixed and the density of the inner fluid is reduced. Moreover, the mechanisms underlying the effect of the Atwood number at the inner interface on the perturbation growth are mainly elucidated by employing the model to analyse each contribution. As the Atwood number decreases, the dominant contribution of the Richtmyer–Meshkov instability is enhanced due to the stronger waves reverberated inside the layer, leading to weakened perturbation growth at initial in-phase interfaces and enhanced perturbation growth at initial anti-phase interfaces.

Key words: shock waves

† Email addresses for correspondence: zzy12@ustc.edu.cn, luoqinliu@ustc.edu.cn

1. Introduction

The hydrodynamic instability of a shock-accelerated finite-thickness fluid layer has great significance in the dynamical characteristics of various phenomena, including inertial confinement fusion (ICF, Betti & Hurricane 2016) and supernova explosions (Arnett *et al.* 1989). Specifically, laser-generated shocks in ICF passing through layers of a capsule containing fusion fuel can lead to capsule material mixing into the fuel (Kishony & Shvarts 2001; Abu-Shawareb *et al.* 2022; Wadas *et al.* 2023), while shocks generated from rapid energy release in core-collapse supernovae propagate outward through the layers of the collapsing stars, causing heavy core elements to jet into outer layers (Kane, Drake & Remington 1999; Hester 2008; Abarzhi *et al.* 2019). Therefore, it is important for scientific and engineering communities to explore the instability evolution of a shock-accelerated finite-thickness fluid layer.

Hydrodynamic instabilities frequently occur on a perturbed interface between two fluids with different densities. They are usually referred to as the Rayleigh–Taylor (RT) instability when the heavy fluid is persistently accelerated by the light one (Rayleigh 1883; Taylor 1950), or the Richtmyer–Meshkov (RM) instability when the interface is subjected to an impulsive force typically by a shock wave (Richtmyer 1960; Meshkov 1969). Both instabilities are induced by the baroclinic vorticity produced by the misaligned directions of density and pressure gradients (Zhou *et al.* 2019, 2021). These instabilities occurring at a shock-accelerated fluid layer in planar geometry depend not only on the fluid-layer thickness and initial layer shape but also the waves reverberated inside the fluid layer. Specifically, the interface coupling effect illustrating the perturbation feedthrough from one interface to another becomes increasingly evident as the initial fluid-layer thickness decreases (Taylor 1950; Mikaelian 1985, 1995; Jacobs *et al.* 1993, 1995; Mikaelian 1996). Also the morphologies of shocked fluid layers are strongly sensitive to the initial layer shape (Jacobs *et al.* 1993, 1995), such that proper perturbations initially imposed at the two interfaces can lead to the freeze out of amplitude where the amplitude growth stagnates (Mikaelian 1995, 1996). In addition, the waves reverberated inside a fluid layer can significantly affect the fluid-layer evolution via the following complicated mechanisms. First, the waves continuously accelerate or decelerate the perturbed interfaces, causing RT destabilization/stabilization effect (Liang *et al.* 2020; Liang & Luo 2021). Second, the waves passing through the perturbed interfaces lead to sudden decreases/increases of amplitudes, which are called compression/decompression effects of waves (Richtmyer 1960; Liang & Luo 2021). Third, additional baroclinic vorticity is deposited on the interface during wave–interface collision to enhance or cancel original vorticity produced by the initial incident shock (Henry de Frahan, Movahed & Johnsen 2015; Liang & Luo 2022*b*; Chen *et al.* 2023*a*,*b*). In recent experiments, it was expected that the Atwood number serves as an important factor for interface coupling effect and reverberating waves (Liang & Luo 2022*a*, 2023). However, the quantitative effect of arbitrary Atwood number on the instability evolution is still not fully understood.

The researches mentioned above have primarily focused on the planar geometry of fluid layers. However, in practical applications such as ICF (Betti & Hurricane 2016) and supernovae (Kane *et al.* 1999), convergent counterparts are more commonly encountered and are of greater practical interest (Mikaelian 1990, 2005; Ding *et al.* 2019; Sun *et al.* 2020; Li *et al.* 2022; Yuan *et al.* 2023; Zhang *et al.* 2023). The instability evolution of a shock-accelerated cylindrical fluid layer with initial perturbations imposed at outer and inner interfaces was investigated by experiments (Ding *et al.* 2019; Sun *et al.* 2020; Li *et al.* 2022). These observations have shown that several factors, including RM instability, RT effect, compressibility effect (Bell 1951; Epstein 2004), Bell–Plesset (BP) effect

(Bell 1951; Plesset 1954) and waves reverberated inside the fluid layer, significantly influence the growth characteristics of the perturbations at shocked cylindrical fluid layers. Zhang *et al.* (2020) modelled the instability evolution of a cylindrical fluid shell in vacuum and found that effects of thin-shell correction and the interface coupling effect are significant to the perturbation growths at thin fluid layers. Recently, Yuan *et al.* (2023) identified various contributions to the perturbation growth at a shock-accelerated cylindrical fluid layer, including RM instability, RT effect, compressibility effect, thin-shell correction, interface coupling effect, compression/decompression effects of reverberated waves and BP effect. Yuan *et al.* (2023) also proposed an improved model by linear combination of the model of Zhang *et al.* (2020) and the compressible Bell model (Bell 1951; Epstein 2004) describing the single interface to quantify all above contributions. Since the interface coupling effect and thin-shell correction in this improved model are formulated based on the assumption of a cylindrical fluid shell in vacuum, the model is only applicable for a shock-accelerated cylindrical fluid layer with high Atwood numbers. However, the Atwood number in applications has a wide range and its effect on the perturbation growth is critical (Amendt *et al.* 2002; Betti & Hurricane 2016; Abu-Shawareb *et al.* 2022). As a result, the underlying mechanisms of Atwood number effects on instability evolution of a shock-accelerated cylindrical fluid layer remains unclear.

In the present work a model is derived theoretically to predict the instability evolution of a shock-accelerated cylindrical fluid layer with arbitrary Atwood numbers. The verification of the model is accomplished by conducting a comparison with direct numerical simulations (DNS) of three fluid-layer configurations in which the outer and intermediate fluids are kept fixed and the density of the inner fluid is reduced. Via the derived model, the mechanisms underlying the effect of the Atwood number at the inner interface on the perturbation growth are elucidated. The remainder of this paper is organized as follows. The derivation of the model is detailed in § 2. The numerical strategy used to simulate the instability evolution is described in § 3. The model validation and the effect of Atwood number are discussed in § 4. The conclusions are addressed in § 5. Furthermore, two additional verification simulations are provided in the Appendix.

2. Modelling of instability evolution

A linear stability analysis is employed here to derive the model describing the perturbation growth at the inner and outer interfaces of a cylindrical fluid layer. As shown in figure 1, a general cylindrical fluid-layer system where two interfaces separate three arbitrary-density fluids $j = A$, B and C at $r > r_1$, $r_1 > r > r_2$ and $r < r_2$, respectively, is considered. Here, r_1 and r_2 represent the radii of unperturbed outer and inner interfaces, respectively. The flow is assumed as potential and, thus, the velocity of fluid j is given as the gradient of the velocity potential ϕ_j. The flow is further assumed as incompressible, such that ϕ_j can be determined by the solution of the Laplace equation

$$\nabla^2 \phi_j = 0. \tag{2.1}$$

Similar to Bell (1951) and Zhang *et al.* (2020), a cosinoidal perturbation is introduced at each interface as

$$r = r_i(t) + \varepsilon \eta_i(t) \cos(n\theta), \tag{2.2}$$

where $\eta_i(t)$ and n denote the perturbation amplitude and wavenumber, respectively. Note that ε is only a formal parameter used to keep the order of the perturbations. Subscripts

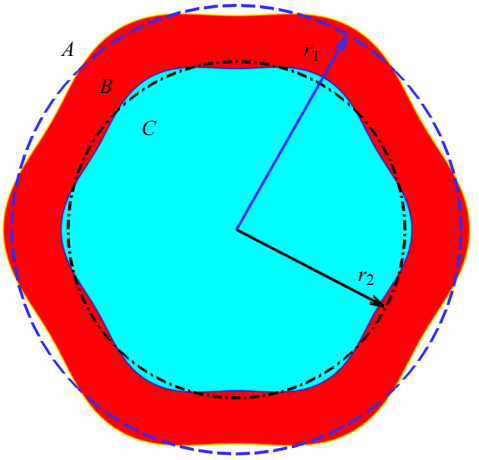

Figure 1. Schematic illustration of a general fluid-layer system including three arbitrary-density fluids A, B and C. Here, r_1 and r_2 are the radial locations of unperturbed outer and inner interfaces, respectively.

$i = 1$ and 2 correspond to the quantities at the outer and inner interfaces, respectively. To the first order of ε, the velocity potential ϕ_j can be derived from (2.1) as

$$\phi_A = r_1\dot{r}_1 \ln r + \varepsilon a(t) r^{-n} \cos(n\theta), \tag{2.3}$$

$$\phi_B = r_i\dot{r}_i \ln r + \varepsilon b(t) r^{n} \cos(n\theta) + \varepsilon c(t) r^{-n} \cos(n\theta), \tag{2.4}$$

$$\phi_C = r_2\dot{r}_2 \ln r + \varepsilon d(t) r^{n} \cos(n\theta), \tag{2.5}$$

where $a(t)$, $b(t)$, $c(t)$ and $d(t)$ are time-dependent functions and the dots represent time derivatives. Note that $i = 1$ or 2 in (2.4). Because the flow is assumed to be incompressible, there is $r_1\dot{r}_1 = r_2\dot{r}_2$ (Zhang *et al.* 2020). At the interface (2.2), the kinematic condition representing the continuity of the velocity component normal to the interface (Mikaelian 1990, 2005) must be satisfied and its linearized formation is as follows:

$$\dot{r}_i + \varepsilon\dot{\eta}_i \cos(n\theta) = \frac{\partial \phi_j}{\partial r}. \tag{2.6}$$

Here, if $i = 1$ then $j = A$ or B, and if $i = 2$ then $j = B$ or C. Substituting (2.3)–(2.5) into (2.6) yields the formulas of $a(t)$, $b(t)$, $c(t)$ and $d(t)$ as follows:

$$a(t) = -\frac{r_1\dot{\eta}_1 + \dot{r}_1\eta_1}{n r_1^{-n}}, \tag{2.7a}$$

$$b(t) = \frac{\dot{\eta}_1 r_1^{n+1} + \dot{r}_1 r_1^{n}\eta_1 - \dot{\eta}_2 r_2^{n+1} - \dot{r}_2 r_2^{n}\eta_2}{n(r_1^{2n} - r_2^{2n})}, \tag{2.7b}$$

$$c(t) = \frac{\dot{\eta}_2 r_2^{-n+1} + \dot{r}_2 r_2^{-n}\eta_2 - \dot{\eta}_1 r_1^{-n+1} - \dot{r}_1 r_1^{-n}\eta_1}{n(r_1^{-2n} - r_2^{-2n})}, \tag{2.7c}$$

$$d(t) = \frac{r_2\dot{\eta}_2 + \dot{r}_2\eta_2}{n r_2^{n}}. \tag{2.7d}$$

Furthermore, the pressure of each fluid can be determined by applying the Bernoulli equation for unsteady potential flow. Thus, the dynamic conditions representing the

continuity of the pressure at the outer and inner interfaces can be expressed as

$$(1-A_{T,1})\left(\frac{\partial\phi_A}{\partial t}+\frac{1}{2}\nabla\phi_A\cdot\nabla\phi_A\right)-(1+A_{T,1})\left(\frac{\partial\phi_B}{\partial t}+\frac{1}{2}\nabla\phi_B\cdot\nabla\phi_B\right)=f_1(t) \quad (2.8)$$

and

$$(1-A_{T,2})\left(\frac{\partial\phi_B}{\partial t}+\frac{1}{2}\nabla\phi_B\cdot\nabla\phi_B\right)-(1+A_{T,2})\left(\frac{\partial\phi_C}{\partial t}+\frac{1}{2}\nabla\phi_C\cdot\nabla\phi_C\right)=f_2(t), \quad (2.9)$$

respectively, where the Atwood number is defined as $A_{T,i}=(\rho_{i,in}-\rho_{i,out})/(\rho_{i,in}+\rho_{i,out})$ with $\rho_{i,in}$ and $\rho_{i,out}$ representing the inner and outer fluid densities of the ith interface, respectively, and $f_1(t)$ and $f_2(t)$ are the time-dependent functions. By substituting (2.3) and (2.4) into (2.8) and substituting (2.4) and (2.5) into (2.9), and then equalizing the coefficients of zeroth-order and first-order terms of ε on both sides of (2.8) and (2.9), f_1, f_2, η_1 and η_2 can be determined. Specifically, $f_1(t)$ and $f_2(t)$ are determined by the coefficients of the zeroth-order terms of ε as $f_1(t)=-2A_{T,1}[(\ddot{r}_1r_1+\dot{r}_1^2)\ln r_1+\dot{r}_1^2/2]$ and $f_2(t)=-2A_{T,2}[(\ddot{r}_2r_2+\dot{r}_2^2)\ln r_2+\dot{r}_2^2/2]$, respectively. The governing equations for η_1 and η_2 are derived from the coefficients of the first-order terms of ε as

$$\begin{aligned}&\frac{(\alpha^{2n}+A_{T,1})(\ddot{r}_1\eta_1+2\dot{r}_1\dot{\eta}_1+r_1\ddot{\eta}_1)-\alpha^n(1+A_{T,1})(r_2\ddot{\eta}_2+2\dot{r}_2\dot{\eta}_2+\ddot{r}_2\eta_2)}{n(\alpha^{2n}-1)}\\&\quad+(1+A_{T,1})\\&\qquad\frac{(\alpha^{-2}-1)(\alpha^{3n}+\alpha^n)(\dot{r}_2\dot{\eta}_2+r_2^{-1}\dot{r}_2^2\eta_2)-(\alpha^{4n}-2\alpha^{2n+2}+1)(\dot{r}_1\dot{\eta}_1+\dot{r}_1^2r_1^{-1}\eta_1)}{(\alpha^{2n}-1)^2}\\&\quad+A_{T,1}\ddot{r}_1\eta_1+(1+A_{T,1})\dot{r}_1\dot{\eta}_1+(1+A_{T,1})\dot{r}_1^2r_1^{-1}\eta_1=0\end{aligned} \quad (2.10)$$

and

$$\begin{aligned}&\frac{\alpha^n(1-A_{T,2})(r_1\ddot{\eta}_1+2\dot{r}_1\dot{\eta}_1+\ddot{r}_1\eta_1)-(\alpha^{2n}-A_{T,2})(\ddot{r}_2\eta_2+2\dot{r}_2\dot{\eta}_2+r_2\ddot{\eta}_2)}{n(\alpha^{2n}-1)}\\&\quad+(1-A_{T,2})\\&\qquad\frac{(\alpha^{3n}+\alpha^n)(\alpha^2-1)(\dot{r}_1\dot{\eta}_1+r_1^{-1}\dot{r}_1^2\eta_1)-(\alpha^{4n}-2\alpha^{2n-2}+1)(\dot{r}_2\dot{\eta}_2+r_2^{-1}\dot{r}_2^2\eta_2)}{(\alpha^{2n}-1)^2}\\&\quad-A_{T,2}\ddot{r}_2\eta_2+(1-A_{T,2})\dot{r}_2\dot{\eta}_2+(1-A_{T,2})\dot{r}_2^2r_2^{-1}\eta_2=0,\end{aligned} \quad (2.11)$$

where $\alpha=r_1/r_2$ is the radius ratio. Note that both (2.10) and (2.11) include $\ddot{\eta}_1$ and $\ddot{\eta}_2$, and thus, cannot individually describe the perturbation growths of the outer and inner interfaces. In order to provide separate descriptions of the perturbation growths of the outer and inner interfaces, $\ddot{\eta}_2$ in (2.10) and $\ddot{\eta}_1$ in (2.11) are eliminated by the linear combinations of (2.10) and (2.11), i.e. $(\alpha^{2n}-A_{T,2})$ (2.10) $-\alpha^n(1+A_{T,1})$ (2.11) and $\alpha^n(1-A_{T,2})$ (2.10) $-(\alpha^{2n}+A_{T,1})$ (2.11), respectively. Then the governing equations for η_1 and η_2 can be

further written as

$$\begin{aligned}
&\frac{\mathrm{d}(r_1^2\dot{\eta}_1)}{\mathrm{d}t} + (nA_{T,1}+1)r_1\ddot{r}_1\eta_1 - \frac{nA_{T,1}A_{T,2}(1+A_{T,1})}{(\alpha^{2n}+A_{T,1}A_{T,2})}r_1\ddot{r}_1\eta_1 \\
&\quad + \frac{n\alpha^{2n}(\alpha^2-1)(1+A_{T,1})(1+A_{T,2})(r_1\dot{r}_1\dot{\eta}_1+\dot{r}_1^2\eta_1)}{(\alpha^{2n}-1)(\alpha^{2n}+A_{T,1}A_{T,2})} \\
&= \frac{n\alpha^{3n+1}(\alpha^2-1)(1+A_{T,1})(1+A_{T,2})\dot{r}_1^2\eta_2}{(\alpha^{2n}-1)(\alpha^{2n}+A_{T,1}A_{T,2})} \\
&\quad - \frac{n\alpha^{n+1}(1+A_{T,1})A_{T,2}r_1\ddot{r}_1\eta_2}{(\alpha^{2n}+A_{T,1}A_{T,2})} + \frac{n\alpha^{n-1}(\alpha^2-1)(1+A_{T,1})(\alpha^{2n}+A_{T,2})r_1\dot{r}_1\dot{\eta}_2}{(\alpha^{2n}-1)(\alpha^{2n}+A_{T,1}A_{T,2})}
\end{aligned} \tag{2.12}$$

and

$$\begin{aligned}
&\frac{\mathrm{d}(r_2^2\dot{\eta}_2)}{\mathrm{d}t} + (nA_{T,2}+1)r_2\ddot{r}_2\eta_2 + \frac{nA_{T,1}A_{T,2}(1-A_{T,2})}{(\alpha^{2n}+A_{T,1}A_{T,2})}r_2\ddot{r}_2\eta_2 \\
&\quad + \frac{n\alpha^{2n-2}(\alpha^2-1)(1-A_{T,1})(1-A_{T,2})(r_2\dot{r}_2\dot{\eta}_2+\dot{r}_2^2\eta_2)}{(\alpha^{2n}-1)(\alpha^{2n}+A_{T,1}A_{T,2})} \\
&= \frac{n\alpha^{3n-3}(\alpha^2-1)(1-A_{T,1})(1-A_{T,2})\dot{r}_2^2\eta_1}{(\alpha^{2n}-1)(\alpha^{2n}+A_{T,1}A_{T,2})} \\
&\quad - \frac{n\alpha^{n-1}A_{T,1}(1-A_{T,2})r_2\ddot{r}_2\eta_1}{(\alpha^{2n}+A_{T,1}A_{T,2})} + \frac{n\alpha^{n-1}(\alpha^2-1)(1-A_{T,2})(\alpha^{2n}-A_{T,1})r_2\dot{r}_2\dot{\eta}_1}{(\alpha^{2n}-1)(\alpha^{2n}+A_{T,1}A_{T,2})},
\end{aligned} \tag{2.13}$$

respectively. The second terms on the left-hand side of (2.12) and (2.13) correspond to the RT effect caused by non-uniform motion of the interface. The third and fourth terms on the left-hand side represent the thin-shell correction. All three terms on the right-hand side of (2.12) and (2.13) are interface coupling effects describing the influences of the perturbation at one interface on that at another. Both the thin-shell correction and interface coupling effect will be insignificant when the thickness increases (i.e. $\alpha \to \infty$). However, it is crucial to consider these two effects in thin fluid layers. When $A_{T,1} = 1$ and $A_{T,2} = -1$, (2.12) and (2.13) are reduced to the model of Zhang *et al.* (2020) describing the instability evolution of a cylindrical fluid shell in vacuum. Therefore, the present model extends the model of Zhang *et al.* (2020) and analytically describes the perturbation growth of an incompressible cylindrical fluid layer with arbitrary Atwood numbers.

Following Ding *et al.* (2017) and Luo *et al.* (2019), the perturbation amplitude can be obtained by integrating (2.12) and (2.13) from t_0 to t twice as

$$\eta_i = \eta_{i,RM} + \eta_{i,RT} + \eta_{i,Thin} + \eta_{i,Cou}. \tag{2.14}$$

Here, $\eta_{i,RM}$ represents the perturbation growth due to RM instability, $\eta_{i,RT}$ is the contribution of the RT effect to the perturbation growth, $\eta_{i,Thin}$ denotes the growth induced by the thin-shell correction and $\eta_{i,Cou}$ represents the contribution of the interface coupling

effect. Specifically,

$$\eta_{i,RM} = \int_{t_0}^{t} \frac{r_{i,t_j^+}^2 \dot{\eta}_{i,t_j^+}}{r_i^2(\tau)} \,\mathrm{d}\tau, \tag{2.15}$$

where r_{i,t_j^+} and $\dot{\eta}_{i,t_j^+}$ in (2.15) represent the position and growth rate of the ith interface at the end moment t_j^+ of the jth wave passing through the interface, and

$$\eta_{i,RT} = \int_{t_0}^{t} -\frac{nA_{T,i}+1}{r_i^2(t')} \int_{t_0}^{t'} r_i(\tau)\ddot{r}_i(\tau)\eta_i(\tau)\,\mathrm{d}\tau\,\mathrm{d}t'. \tag{2.16}$$

Terms $\eta_{1,Thin}$ and $\eta_{2,Thin}$ take forms as

$$\begin{aligned}\eta_{1,Thin} = \int_{t_0}^{t} \frac{1}{r_1^2(t')} \Bigg\{ &\int_{t_0}^{t'} \frac{nA_{T,1}A_{T,2}(1+A_{T,1})}{\alpha^{2n}(\tau)+A_{T,1}A_{T,2}} r_1(\tau)\ddot{r}_1(\tau)\eta_1(\tau)\,\mathrm{d}\tau \\ &- \int_{t_0}^{t'} \frac{n\alpha^{2n}(\tau)[\alpha^2(\tau)-1](1+A_{T,1})(1+A_{T,2})}{[\alpha^{2n}(\tau)-1][\alpha^{2n}(\tau)+A_{T,1}A_{T,2}]} r_1(\tau)\dot{r}_1(\tau)\dot{\eta}_1(\tau)\,\mathrm{d}\tau \\ &- \int_{t_0}^{t'} \frac{n\alpha^{2n}(\tau)[\alpha^2(\tau)-1](1+A_{T,1})(1+A_{T,2})}{[\alpha^{2n}(\tau)-1][\alpha^{2n}(\tau)+A_{T,1}A_{T,2}]} \dot{r}_1^2(\tau)\eta_1(\tau)\,\mathrm{d}\tau \Bigg\}\,\mathrm{d}t' \end{aligned} \tag{2.17}$$

and

$$\begin{aligned}\eta_{2,Thin} = \int_{t_0}^{t} \frac{1}{r_2^2(t')} \Bigg\{ &- \int_{t_0}^{t'} \frac{nA_{T,1}A_{T,2}(1-A_{T,2})}{\alpha^{2n}(\tau)+A_{T,1}A_{T,2}} r_2(\tau)\ddot{r}_2(\tau)\eta_2(\tau)\,\mathrm{d}\tau \\ &- \int_{t_0}^{t'} \frac{n\alpha^{2n-2}(\tau)[\alpha^2(\tau)-1](1-A_{T,1})(1-A_{T,2})}{[\alpha^{2n}(\tau)-1][\alpha^{2n}(\tau)+A_{T,1}A_{T,2}]} r_2(\tau)\dot{r}_2(\tau)\dot{\eta}_2(\tau)\,\mathrm{d}\tau \\ &- \int_{t_0}^{t'} \frac{n\alpha^{2n-2}(\tau)[\alpha^2(\tau)-1](1-A_{T,1})(1-A_{T,2})}{[\alpha^{2n}(\tau)-1][\alpha^{2n}(\tau)+A_{T,1}A_{T,2}]} \dot{r}_2^2(\tau)\eta_2(\tau)\,\mathrm{d}\tau \Bigg\}\,\mathrm{d}t', \end{aligned} \tag{2.18}$$

respectively. Terms $\eta_{1,Cou}$ and $\eta_{2,Cou}$ are read as

$$\begin{aligned}\eta_{1,Cou} = \int_{t_0}^{t} \frac{1}{r_1^2(t')} \Bigg\{ &- \int_{t_0}^{t'} \frac{n\alpha^{n+1}(\tau)(1+A_{T,1})A_{T,2}}{\alpha^{2n}(\tau)+A_{T,1}A_{T,2}} r_1(\tau)\ddot{r}_1(\tau)\eta_2(\tau)\,\mathrm{d}\tau \\ &+ \int_{t_0}^{t'} \frac{n\alpha^{n-1}(\tau)[\alpha^2(\tau)-1](1+A_{T,1})[\alpha^{2n}(\tau)+A_{T,2}]}{[\alpha^{2n}(\tau)-1][\alpha^{2n}(\tau)+A_{T,1}A_{T,2}]} r_1(\tau)\dot{r}_1(\tau)\dot{\eta}_2(\tau)\,\mathrm{d}\tau \\ &+ \int_{t_0}^{t'} \frac{n\alpha^{3n+1}(\tau)[\alpha^2(\tau)-1](1+A_{T,1})(1+A_{T,2})}{[\alpha^{2n}(\tau)-1][\alpha^{2n}(\tau)+A_{T,1}A_{T,2}]} \dot{r}_1^2(\tau)\eta_2(\tau)\,\mathrm{d}\tau \Bigg\}\,\mathrm{d}t' \end{aligned} \tag{2.19}$$

and

$$\eta_{2,Cou} = \int_{t_0}^{t} \frac{1}{r_2^2(t')} \left\{ - \int_{t_0}^{t'} \frac{n\alpha^{n-1}(\tau)A_{T,1}(1-A_{T,2})}{\alpha^{2n}(\tau)+A_{T,1}A_{T,2}} r_2(\tau)\ddot{r}_2(\tau)\eta_1(\tau)\,\mathrm{d}\tau \right.$$
$$+ \int_{t_0}^{t'} \frac{n\alpha^{n-1}(\tau)[\alpha^2(\tau)-1](1-A_{T,2})[\alpha^{2n}(\tau)-A_{T,1}]}{[\alpha^{2n}(\tau)-1][\alpha^{2n}(\tau)+A_{T,1}A_{T,2}]} r_2(\tau)\dot{r}_2(\tau)\dot{\eta}_1(\tau)\,\mathrm{d}\tau$$
$$\left. + \int_{t_0}^{t'} \frac{n\alpha^{3n-3}(\tau)[\alpha^2(\tau)-1](1-A_{T,1})(1-A_{T,2})}{[\alpha^{2n}(\tau)-1][\alpha^{2n}(\tau)+A_{T,1}A_{T,2}]} \dot{r}_2^2(\tau)\eta_1(\tau)\,\mathrm{d}\tau \right\} \mathrm{d}t', \quad (2.20)$$

respectively.

It is worth noting that (2.14) derived within the framework of the incompressible potential flow inherently disregards the compressibility effect and the compression and/or decompression effect of waves. Here, the compressibility effect refers to the effect of fluid compression caused by the basic flow to the centre of cylindrical geometry (Bell 1951; Epstein 2004). Moreover, the compression or decompression effect of waves denotes the sudden decrease/increase in the perturbation amplitude during the wave passing through the interface (Richtmyer 1960; Liang & Luo 2021). Evidently, these two effects describe distinct physical processes compared with the incompressible model and make noteworthy contributions to perturbation growth on the cylindrical interface (Luo *et al.* 2019; Yuan *et al.* 2023; Zhang *et al.* 2023). These two effects can be modelled as following two terms. Specifically, according to Bell (1951) and Epstein (2004), the compressibility effect caused by the base flow to the centre after the impact of the incident shock can be modelled as

$$\eta_{i,Com} = \int_{t_0}^{t} \frac{c_i}{r_i^2(t')} \left[\int_{t_0}^{t'} r_i(\tau)\dot{r}_i(\tau)\eta_i(\tau)\,\mathrm{d}\tau + \int_{t_0}^{t'} r_i^2(\tau)\dot{\eta}_i(\tau)\,\mathrm{d}\tau \right] \mathrm{d}t', \quad (2.21)$$

where the parameter $c_i = -\dot{\rho}_{i,in}/\rho_{i,in} = -\dot{\rho}_{i,out}/\rho_{i,out}$ is the expansion rate of the species at the ith interface. The expansion rate can be approximated as a constant value, $c_i \approx [(r_{i,min}/r_{i,0})^2 - 1]/t_{res}$ (Luo *et al.* 2019; Wu, Liu & Xiao 2021), where $r_{i,min}$ denotes the smallest radius of the ith interface during its motion, $r_{i,0}$ is the initial position of the ith interface and t_{res} represents the time when the reshock happens. Moreover, the compression/decompression effect represents the sudden decrease/increase of the perturbation amplitude of the interface impacted by one known wave (Richtmyer 1960; Liang & Luo 2021). For a shock-accelerated fluid layer, the inner and outer interfaces are successively impacted by several waves as a result of reverberations inside the layer. The overall variations of the perturbation amplitudes on the interfaces caused by the compression/decompression effects of the successive waves can be modelled by accumulating every rapid decrease/increase of the amplitude induced by each wave (Yuan *et al.* 2023),

$$\eta_{i,CD} = \eta_{i,t_0} + \int_{t_0}^{t} \frac{\Delta V(\tau)}{2}\,\mathrm{d}\tau, \quad (2.22)$$

where η_{i,t_0} is the initial amplitude of the ith interface at t_0. The function $\Delta V(\tau)$ defined in (2.22) represents the radial velocity jump of the unperturbed interface at the moment τ, namely if $t_j^- < \tau < t_j^+$, $\Delta V(\tau) = \pm|\Delta V_j|$, otherwise $\Delta V(\tau) = 0$. Here, ΔV_j is the jth radial velocity jump of the interface impacted by the jth wave reverberated inside the fluid layer, t_j^- and t_j^+ are the beginning and end moments of the jth wave passing through the

interface and the operators '+' and '−' before the term $|\Delta V_j|$ represent decompression and compression effects.

Typically, the terms describing the above two effects are linearly superimposed on incompressible models, and it has been demonstrated that the resulting superimposed model effectively describes the instability evolution on cylindrical interfaces. Specifically, via a comparative analysis of compressible and incompressible models of instability evolution for the cylindrical interface (Bell 1951; Epstein 2004; Luo *et al.* 2019; Zhang *et al.* 2023), the term (2.21) describing the compressibility effect resulting from the base flow towards the centre can be linearly superimposed on the incompressible model. Moreover, the term (2.22) modelling the compression/decompression effect of waves has been linearly superimposed on the incompressible model by Zhang *et al.* (2023) to effectively describe instability evolution in the heavy fluid layer impacted by a divergent shock. To this end, the terms (2.21) and (2.22) are linearly superimposed on (2.14) as

$$\eta_i = \eta_{i,RM} + \eta_{i,RT} + \eta_{i,Thin} + \eta_{i,Cou} + \eta_{i,Com} + \eta_{i,CD}, \tag{2.23}$$

thereby improving the incompressible model to predict the perturbation growth on a shock-accelerated cylindrical fluid layer with arbitrary Atwood numbers. It is possible to model the perturbation growth in this linear superposition because each contribution in the model (2.23) represents an independent physical mechanism responsible for the perturbation growth (Bell 1951; Epstein 2004; Zhang *et al.* 2020). Moreover, the incompressible terms (2.14) are derived from the linear stability analysis, which assumes the perturbation amplitudes to be small ($\eta_i/\lambda_i \lesssim 0.1$) (Bell 1951; Epstein 2004). Therefore, the nonlinear effects associated with the higher-order terms of amplitude can be disregarded and are not considered in the contributions at the linear stage of the perturbation growth.

It is important to note that the use of the present model (2.23) requires obtaining the ith interface's trajectory $r_i(t)$, post-shock Atwood number $A_{T,i}$, expansion rate c_i and the velocity jump induced by the jth wave ΔV_j from the base flow, i.e. shock-accelerated unperturbed cylindrical fluid layer (Wu *et al.* 2021). Moreover, the beginning t_j^- and end t_j^+ moments of the jth wave passing through the perturbed interface and the growth rate $\dot{\eta}_{i,t_j^+}$ of the perturbation on the ith interface at t_j^+ need to be obtained from numerical or experimental data (Ding *et al.* 2017; Wu *et al.* 2021; Yuan *et al.* 2023; Zhang *et al.* 2023). According to previous work (Luo *et al.* 2019; Zou *et al.* 2019; Wu *et al.* 2021), the impact of shock waves on the interface causes rapid changes in the amplitude and growth rate of the perturbation at the interface. To include the effect of shock wave interaction on the growth rate, the integrals in the model are performed piecewise in the time between wave interactions and the growth rate in the RM term $\eta_{i,RM}$ is updated from the DNS results at time t_j^+. The change in perturbation amplitude caused by the impact of a shock wave is modelled by the compression/decompression term $\eta_{i,CD}$. Consequently, the present model (2.23) is capable of describing the entire process of the instability evolution in a shock-accelerated cylindrical fluid layer.

3. Numerical methods

3.1. *Governing equations*

Direct numerical simulation has been performed to obtain the instability evolution of the shock-accelerated fluid layer in cylindrical geometry and then to validate the present model (2.23). The pressure p_A^* and density ρ_A^* of unshocked outer fluid A, as shown in figure 1,

are chosen as the characteristic scales. Here, the characteristic velocity and temperature are described, respectively, as $u_A^* = \sqrt{p_A^*/\rho_A^*}$ and $T_A^* = p_A^* M_A^*/(R^* \rho_A^*)$ with the universal gas constant R^* and fluid A's molar mass M_A^*. Hereafter, the superscript '$*$' denotes the dimensional physical quantity and the subscript 'A' corresponds to the quantity of unshocked fluid A. The radius of the unperturbed outer interface r_1^* has been used as the characteristic length. Thus, the non-dimensionalized governing equations in cylindrical coordinates (r, θ) are

$$\frac{\partial \rho}{\partial t} + \boldsymbol{\nabla}\cdot(\rho \boldsymbol{u}) = 0, \tag{3.1}$$

$$\frac{\partial (\rho \boldsymbol{u})}{\partial t} + \boldsymbol{\nabla}\cdot(\rho \boldsymbol{u}\boldsymbol{u}) = -\boldsymbol{\nabla} p + \frac{1}{Re}\boldsymbol{\nabla}\cdot\boldsymbol{\tau}, \tag{3.2}$$

$$\frac{\partial (\rho E)}{\partial t} + \boldsymbol{\nabla}\cdot[(\rho E + p)\boldsymbol{u}] = \frac{1}{Re}\boldsymbol{\nabla}\cdot(\boldsymbol{\tau}\cdot\boldsymbol{u}) - \frac{1}{RePr}\boldsymbol{\nabla}\cdot\boldsymbol{q}_c - \frac{1}{ReSc}\boldsymbol{\nabla}\cdot\boldsymbol{q}_d, \tag{3.3}$$

$$\frac{\partial (\rho Y_i)}{\partial t} + \boldsymbol{\nabla}\cdot(\rho Y_i \boldsymbol{u}) = -\frac{1}{ReSc}\boldsymbol{\nabla}\cdot\boldsymbol{J}_i, \quad i = A, B, \tag{3.4}$$

where ρ is the fluid density; $\boldsymbol{u} = (u_r, u_\theta)$ denotes the velocity vector; p is the pressure; $E = C_v T + \boldsymbol{u}\cdot\boldsymbol{u}/2$ denotes the specific total energy with the specific heat at constant volume C_v and the temperature T; $Y_A = \rho_A/\rho$ and $Y_B = \rho_B/\rho$ are the species mass fractions of fluids A and B, respectively, and $Y_C = 1 - Y_A - Y_B$ is the species mass fraction of fluid C; and the symbol $\boldsymbol{\nabla}$ denotes the vector-differentiation operator. The stress tensor is obtained as $\boldsymbol{\tau} = 2\mu\boldsymbol{S} - 2\mu/3(\boldsymbol{\nabla}\cdot\boldsymbol{u})\boldsymbol{\delta}$, where μ is the dynamic viscosity, $\boldsymbol{S} = (\boldsymbol{\nabla}\boldsymbol{u} + (\boldsymbol{\nabla}\boldsymbol{u})^T)/2$ is the strain-rate tensor and $\boldsymbol{\delta}$ represents the unit tensor. The heat fluxes due to heat conduction ($\boldsymbol{q}_c$) and interspecies enthalpy diffusion ($\boldsymbol{q}_d$) are given by $\boldsymbol{q}_c = -\gamma_A/[M_A(\gamma_A - 1)]\kappa\boldsymbol{\nabla}T$ and $\boldsymbol{q}_d = \sum_i h_i \boldsymbol{J}_i (i = A, B, C)$, respectively, where γ_A is the ratio of specific heats of fluid A, M_A is the molar mass of fluid A, κ is the heat conduction coefficient, h_i is the enthalpy, $\boldsymbol{J}_i = -\rho D \boldsymbol{\nabla} Y_i$ is the diffusive mass flux obtained by the Fick law and D is the diffusion coefficient. The above governing equations are closed with the non-dimensionalized ideal gas equation of state, i.e. $p = \rho T/M$, where M is the molar mass. Based on $\sum_i Y_i = 1$, the summation of the species mass fraction transport equations of all species given by (3.4) can be reasonably recovered as the continuity equation (3.1) for the mixture density. Moreover, the same difference scheme should be used to approximate $\boldsymbol{\nabla} Y_i$ for each species, ensuring that the numerical simulation satisfies $\sum_i(\boldsymbol{\nabla}\cdot\boldsymbol{J}_i) = 0$.

Following Ge *et al.* (2022), the density and pressure of the mixture are obtained by the summation of each species, while the temperature is equal for each species of the mixture. Therefore, the molecular mass of the mixture is given by $M = (\sum Y_i/M_i)^{-1}$, where M_i is the molecular mass of the ith species. The quantities describing the physical properties of the mixture, such as the dynamic viscosity μ, the diffusion coefficient D, the heat conduction coefficient κ, the specific heat at constant pressure C_p and the specific heat at constant volume C_v, are calculated by the linear combinations of each species weighted with their mass fractions. The dynamic viscosity of the ith species μ_i is computed by the Sutherland law as

$$\mu_i = \frac{\mu_{0,i}^*}{\mu_A^*}\left(\frac{T_A^* T}{T_0^*}\right)^{3/2}\frac{T_0^* + T_s^*}{T_A^* T + T_s^*}, \tag{3.5}$$

where $T_s^* = 124$ K and $\mu_{0,i}^*$ is the dynamic viscosity at the reference temperature $T_0^* = 273.15$ K. The heat conduction coefficient κ_i and diffusion coefficient D_i of the ith species can be obtained by the constant Prandtl number, $Pr_i = C_{p,i}^* \mu_i^*/\kappa_i^*$, and the constant Schmidt number, $Sc_i = \mu_i^*/(\rho_i^* D_i^*)$, respectively. The specific heat at constant pressure

Species	ρ_i^* (kg m^{-3})	p_i^* (kPa)	T_i^* (K)	γ_i	Pr_i	Sc_i	M_i^* (g mol^{-1})	$\mu_{0,i}^*$ (kg m^{-1} s^{-1})
Ne	0.83	101.325	298	1.68	0.67	0.676	20.18	1.4757×10^{-5}
Air	1.18	101.325	298	1.40	0.72	0.757	28.96	1.7161×10^{-5}
CO_2	1.80	101.325	298	1.31	0.77	0.766	44.01	1.3711×10^{-5}
Kr	3.43	101.325	298	1.67	0.67	0.674	83.80	2.3219×10^{-5}
SF_6	5.98	101.325	298	1.09	0.80	0.691	146.06	1.2388×10^{-5}

Table 1. Initial unshocked parameters of the species. Here the subscript $i = N, A, C, K$ and S represents the species Ne (Neon), air, CO_2 (Carbon Dioxide), Kr (Krypton) and SF_6 (Sulphur hexafluoride), respectively.

can be calculated by $C_{p,i}^* = \gamma_i R^*/[(\gamma_i - 1)M_i^*]$. Moreover, the parameters of fluids to obtain the quantities describing the mixture properties are listed in table 1. Note that the present model (2.23) based on the potential flow assumption is suitable for describing the instability evolutions of shock-accelerated fluid layers without viscosity or with high Reynolds number. However, to get closer to the interfacial instability in real applications or experiments, the gases with real parameters are selected for the simulation and the viscosity of gas is included.

The non-dimensional parameters in (3.1)–(3.4) are the Reynolds, Prandtl and Schmidt numbers defined, respectively, as

$$Re = \frac{\rho_A^* u_A^* r_1^*}{\mu_A^*}, \quad Pr = \frac{C_{p,A}^* \mu_A^*}{\kappa_A^*}, \quad Sc = \frac{\mu_A^*}{\rho_A^* D_A^*}. \tag{3.6a–c}$$

In the present study the outer fluid A and intermediate fluid B in figure 1 are fixed to air and SF_6, respectively, to keep the same strength of incident shock wave and Atwood number at the outer interface $A_{T,1}$. Therefore, the physical quantities of unshocked air are chosen as the characteristic scales. Thus, the Prandtl and Schmidt numbers in governing equations are 0.72 and 0.757, respectively. A sufficiently high Reynolds number is set as 10^5 to avoid the effects of viscosity, heat conduction and interfacial diffusion on the instability evolution (Walchli & Thornber 2017).

A numerical algorithm of high-order finite difference schemes is used to solve the governing equations (3.1)–(3.4) in cylindrical coordinates. Specifically, the seventh-order weighted essentially non-oscillatory scheme is implemented to discretize the convective terms. The eighth-order central difference scheme is performed to discretize the viscous terms. The time derivative is approximated by the classical third-order Runge–Kutta method. To validate the present numerical algorithm, the RM instability of the cylindrical air/SF_6 interface accelerated by an incident shock with the shock Mach number $Ma = 1.25$ is simulated and compared with the DNS results from Wu *et al.* (2021). The initial perturbation amplitude $a_0 = 0.025$ and the premixed thickness of the interface $\delta = 0.025$ are consistent with the parameters used by Wu *et al.* (2021). Figure 2 clearly demonstrates that the evolution of the perturbation amplitude in the present study is in excellent agreement with the DNS results reported by Wu *et al.* (2021). This agreement serves as validation, indicating that the DNS utilized in the current work effectively captures the perturbation growth in a shock-accelerated cylindrical interface. The above numerical algorithm to simulate the instability evolution has also been well validated in previous studies (Zhao *et al.* 2020; Fu *et al.* 2022; Yuan *et al.* 2023).

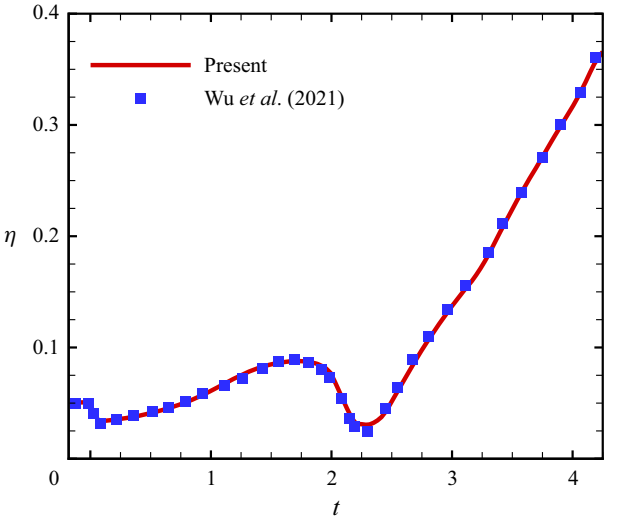

Figure 2. Evolution of the perturbation amplitude (red solid line) for the single-mode cylindrical RM instability at the initial perturbation amplitude $a_0 = 0.025$ and the premixed thickness of the interface $\delta = 0.025$ in comparison with the numerical data (blue squares) (Wu *et al.* 2021).

3.2. *Problem set-up*

The shape function of a cosinoidally perturbed interface is defined as $\zeta_i(\theta) = r_i + a_i \cos(n\theta)$ $(i = 1, 2)$, where a_i and n are the initial amplitude and wavenumber, respectively. Notably, the amplitude is set as $a_i = 0$ for an unperturbed interface. By introducing the error function to smooth the interfaces, the mass fraction fields of fluids A and B are initialized as

$$Y_A(r, \theta; t = 0) = \frac{1}{2}\left[1 + erf\left(\frac{r - \zeta_1(\theta)}{\delta}\right)\right], \tag{3.7a}$$

$$Y_B(r, \theta; t = 0) = \frac{1}{2}\left[erf\left(\frac{r - \zeta_2(\theta)}{\delta}\right) - erf\left(\frac{r - \zeta_1(\theta)}{\delta}\right)\right], \tag{3.7b}$$

respectively, where $\delta = 0.005$ is the initial premixed thickness of the interface, which is low enough to ignore the interfacial diffusion (Walchli & Thornber 2017). The incident shock with shock Mach number $Ma = 1.25$ is initially at $r_s = 1.25$ for consistency with the experiments (Ding *et al.* 2019; Sun *et al.* 2020) and simulations (Wu *et al.* 2021; Li *et al.* 2022). The present work assumes a uniform pressure $p = 1$ and temperature $T = 1$ in unshocked regions. The initialization of the post-shock fluid is supposed to be uniform and calculated using the Rankine–Hugoniot conditions (Wu *et al.* 2021; Li *et al.* 2022; Yan *et al.* 2022).

The shocked fluid layer is numerically investigated within a two-dimensional circular domain $D = \{(r, \theta) | r_{in} \leqslant r \leqslant r_{out}, 0 \leqslant \theta < 2\pi\}$. To avoid a pole singularity at the centre of the cylindrical coordinates, a micro-hole with a radius $r_{in} = 0.01$ is dug out. This strategy has been commonly verified to have little influence on the interfacial instability evolution (Zhao *et al.* 2020; Wu *et al.* 2021). In addition, in order to eliminate effects of reflected waves from the exterior boundary, a sufficiently long sponge layer with a radial width of approximately $19r_{out}$ is added at $r > r_{out} = 1.5$. Following previous work (Lombardini, Pullin & Meiron 2014; Wu *et al.* 2021), a reflective wall boundary condition is applied to the interior boundary at $r = r_{in}$, where the velocity and the gradients of the

Layer	Interface	Type	$A_{T,i}$	c_i	ΔV_1	ΔV_2	ΔV_r
ASK	II_1	air/SF_6	0.706	−0.482	−0.330	−0.032	0.369
	II_2	SF_6/Kr	−0.375	−0.550	−0.355	−0.007	0.264
ASC	II_1	air/SF_6	0.706	−0.592	−0.330	−0.118	0.374
	II_2	SF_6/CO_2	−0.572	−0.718	−0.424	−0.043	0.270
ASN	II_1	air/SF_6	0.706	−0.706	−0.330	−0.171	0.321
	II_2	SF_6/Ne	−0.789	−0.847	−0.467	−0.062	0.192

Table 2. Detailed parameters corresponding to the base flow of different fluid layers. Here $A_{T,i}$ is the post-shock Atwood number, c_i denotes the expansion rate of the species, ΔV_j represents the jth jump of interfacial inward velocity before reshock and ΔV_r denotes the jump induced by the reshock.

density, temperature and species mass fractions are set to zero. A type of non-reflecting boundary condition is prescribed on the exterior boundary at $r = 20r_{out}$, where the numerical fluxes of the waves propagating out of the domain are extrapolated from the solution within the domain while those propagating into the domain are set to zero. In fact, the outward-moving reflected shocks formed by the collision of the incident shock on the fluid layer do not reach the exterior boundary at $r = 20r_{out}$ until the end of the simulation. Hence, the boundary conditions at the exterior side have a negligible impact on the current numerical results. In the present study the initial ratio α_0 has been set as 1.1 and the fluid layer is thin enough to have an obvious interface coupling effect (Zhang *et al.* 2020). It is noted that all the simulations are performed on the grid resolution of 1200^2, which has been confirmed to well capture the essential flow dynamics in instability evolution on shocked heavy fluid layers (Yuan *et al.* 2023).

4. Validation and discussion

To validate the model (2.23), three cylindrical fluid-layer configurations, i.e. air/SF_6/Kr (ASK) layer, air/SF_6/CO_2 (ASC) layer and air/SF_6/Ne (ASN) layer have been simulated. For these three configurations, the outer fluid A and intermediate fluid B in figure 1 are fixed to air and SF_6, respectively, to ensure that the strength of the incident shock wave and Atwood number at the outer interface $A_{T,1}$ are the same in each simulated case. The inner fluid C in figure 1 is set to Kr, CO_2 and Ne, to verify the applicability of model (2.23) to various Atwood numbers at the inner interface and to further investigate the effect of Atwood number on the shock-accelerated cylindrical fluid layer. Moreover, the validations of the model's applicability to various Atwood numbers at the outer interface are presented in the Appendix.

4.1. *Base flow*

The flow field behind a converging shock is non-uniform as the converging shock travels to the geometry centre (Chisnell 1998), and hence, no analytical solution exists for the base flow of a shock-accelerated cylindrical fluid layer (Luo *et al.* 2019). Therefore, an initially unperturbed fluid layer impacted by a concentric shock must be firstly examined to provide a base flow. The parameters of the ASK, ASC and ASN layers are listed in table 2. For these three layers, $A_{T,1}$ is fixed at 0.706 and $A_{T,2}$ decreases from −0.375 to −0.572 and −0.789. Since the evolutions of interfaces and waves are qualitatively the same in the three layers, the ASC layer is taken as an example to detail the wave patterns and interface motions of the shock-accelerated cylindrical fluid layer.

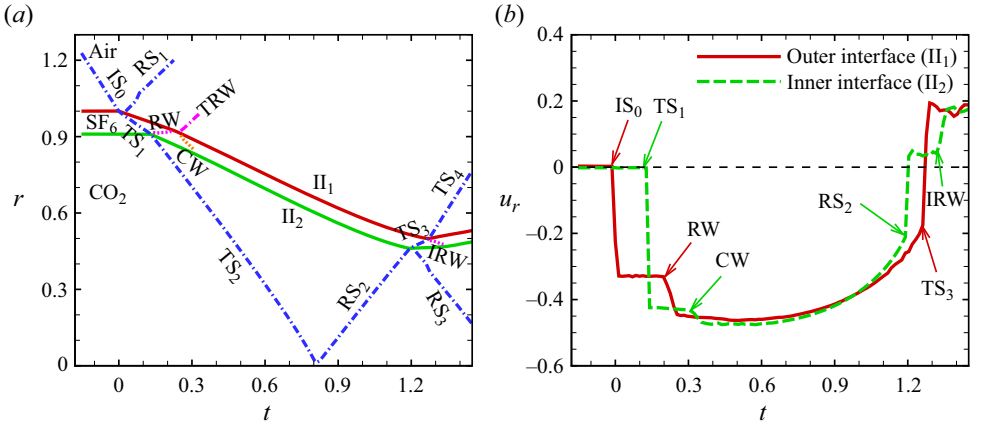

Figure 3. Temporal variations of (*a*) radial positions of interfaces and waves and of (*b*) radial velocities of interfaces at which the circular IS_0 impacts upon the unperturbed ASC layer with $\alpha_0 = 1.1$. Notation: IS_0, incident shock; II_1, outer interface; II_2, inner interface; RS_i, ith reflected shock; TS_i, ith transmitted shock; RW, rarefaction wave; TRW, transmitted rarefaction wave; CW, compression wave; IRW, inward-moving rarefaction wave.

The quantitative descriptions for positions of waves and interfaces and for radial velocities (u_r) of interfaces are displayed in figure 3. Note that the temporal origin is defined as the moment when the incident shock (IS_0) meets the outer interface (II_1). As the IS_0 travels inwards and collides with II_1, it bifurcates into an inward-moving transmitted shock (TS_1) and an outward-moving reflected shock (RS_1). Impacted by IS_0, II_1 speeds up rapidly and then starts to move inwards at a nearly constant speed. Then, TS_1 colliding with the inner interface (II_2) generates a second inward-moving transmitted shock (TS_2) and an outward-moving rarefaction wave (RW) since II_2 is a heavy/light interface relative to the motion of TS_1. Accelerated by TS_1, II_2 has a rapid decrease of velocity and starts to move inwards as shown in figure 3(*b*). The outward-moving RW impacts upon II_1, leading to a velocity jump of II_1 due to the fact that the pressure behind the RW front is lower than that before the RW front (Liang *et al.* 2020). Meanwhile, since II_1 is a heavy/light interface relative to the motion of RW, a transmitted rarefaction wave (TRW) is refracted outside the fluid layer and an inward-moving compression wave (CW) is reflected to collide with II_2, resulting in a velocity increase of II_2. Theoretically, the above wave propagation will be reverberated many times inside the fluid layer. However, after the CW collides with II_2, the waves reverberated inside the fluid layer are too weak to influence the interface velocity and can be ignored. Later, an outward-moving shock (RS_2) is reflected to expand outwards when TS_2 focuses at the geometry centre. At the same time, two interfaces slow down gradually due to the compressibility of the inner species and the effect of the RS_2 (Wu *et al.* 2021). Impacting with II_2, RS_2 bifurcates into an outward-moving transmitted shock (TS_3) and an inward-moving reflected shock (RS_3). Soon, TS_3 colliding with II_1 generates an outward-moving transmitted shock (TS_4) and reflects an inward-moving rarefaction wave (IRW). As indicated by figure 3(*b*), RS_2 impacting upon II_2 and TS_3 colliding with II_1 cause another velocity jump at II_2 and II_1, respectively.

The necessary physical quantities to employ the model (2.23) to predict the perturbation growth can be obtained via the base flow, including the interfacial trajectory $r_i(t)$, the post-shock Atwood number $A_{T,i}$, the expansion rate c_i and the value of the interface's jth velocity jump ΔV_j induced by the jth wave, which are listed in table 2. Note that the Atwood number at the inner interface $A_{T,2}$ has significant effects on the velocity

Layer	Interface	Type	a_1/λ_1	a_2/λ_2	n	t_1^-	t_1^+	$\dot{\eta}_{i,t_1^+}$	t_2^-	t_2^+	$\dot{\eta}_{i,t_2^+}$
ASK6	II_1	air/SF_6	0.02	0.02	6	−0.014	0.014	0.006	0.211	0.225	0.015
	II_2	SF_6/Kr	0.02	0.02	6	0.112	0.140	0.004	—	0.310	0.012
ASC6	II_1	air/SF_6	0.02	0.02	6	−0.014	0.014	0.006	0.225	0.239	0.010
	II_2	SF_6/CO_2	0.02	0.02	6	0.112	0.140	0.003	—	0.336	0.005
ASN6	II_1	air/SF_6	0.02	0.02	6	−0.014	0.014	0.006	0.234	0.245	0.002
	II_2	SF_6/Ne	0.02	0.02	6	0.112	0.137	−0.001	—	0.380	−0.008
ASC12	II_1	air/SF_6	0.02	0.02	12	0	0.014	0.008	—	0.309	0.015
	II_2	SF_6/CO_2	0.02	0.02	12	0.126	0.140	0.001	—	0.365	−0.004

Table 3. Detailed parameters corresponding to the IP cases. Here, a_i is initial amplitude, λ_i is initial wavelength, n is the wavenumber of the perturbed interface, t_j^- and t_j^+ are the beginning and end moments of the jth wave passing through the interface, $\dot{\eta}_{i,t_j^+}$ represents the growth rate of the II_i at t_j^+.

Layer	Interface	Type	a_1/λ_1	a_2/λ_2	n	t_1^-	t_1^+	$\dot{\eta}_{i,t_1^+}$	t_2^-	t_2^+	$\dot{\eta}_{i,t_2^+}$
ASK6	II_1	air/SF_6	0.02	−0.02	6	−0.014	0.014	0.006	0.126	0.310	0.050
	II_2	SF_6/Kr	0.02	−0.02	6	0.084	0.168	0.010	0.182	0.310	0.042
ASC6	II_1	air/SF_6	0.02	−0.02	6	−0.014	0.014	0.006	0.126	0.334	0.074
	II_2	SF_6/CO_2	0.02	−0.02	6	0.084	0.168	0.018	0.182	0.306	0.078
ASN6	II_1	air/SF_6	0.02	−0.02	6	−0.014	0.014	0.006	0.118	0.308	0.110
	II_2	SF_6/Ne	0.02	−0.02	6	0.084	0.174	0.030	0.185	0.256	0.115
ASC12	II_1	air/SF_6	0.02	−0.02	12	0	0.014	0.008	0.183	0.280	0.052
	II_2	SF_6/CO_2	0.02	−0.02	12	0.112	0.155	0.010	0.225	0.280	0.052

Table 4. Detailed parameters corresponding to the AP cases. Notations can be found in table 3.

jumps. Specifically, as $A_{T,2}$ decreases, the increase of density difference at II_2 leads to a corresponding increase in the absolute value $|\Delta V_1|$ of II_2 impacted by TS_1. Moreover, the absolute values $|\Delta V_2|$ of II_1 induced by the RW and of II_2 induced by the CW are also more prominent. This is due to the fact that the RW and CW are enhanced as $A_{T,2}$ decreases and the density difference at II_2 increases.

4.2. *Validation of the model*

Following the experiments of Liang & Luo (2022*a*), two typical cases in which the phase differences between two perturbed interfaces are 0 and π, corresponding to in-phase (IP) cases and anti-phase (AP) cases, respectively, are performed to examine the instability evolutions of the three layers. The ratio of initial perturbation amplitude to wavelength is fixed at 0.02 to satisfy the small-perturbation assumption, and two wavenumbers are chosen as $n = 6$ and 12 to verify the applicability of the model to various wavenumbers. The perturbation amplitude η_i is defined as $\eta_i = (r_{\theta=0} - r_{\theta=\pi/n})/2 (i = 1, 2)$ with $r_{\theta=0}$ and $r_{\theta=\pi/n}$ representing the radial locations where $Y_{SF_6} = 0.5$ along $\theta = 0$ and $\theta = \pi/n$ lines, respectively. Further details of the IP cases and AP cases used in this work are listed in tables 3 and 4, respectively, including the beginning t_j^- and end t_j^+ moments of the jth wave passing through the interface and the perturbation growth rate at t_j^+, which are necessary for the employment of the model.

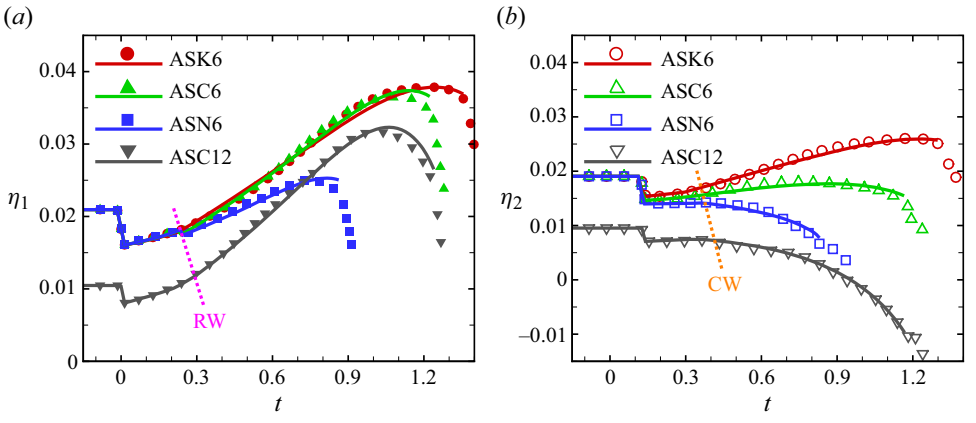

Figure 4. Temporal variations of the amplitudes of the outer (η_1) and inner (η_2) interfaces for the IP cases. The simulation data are marked by symbols and the model results are denoted by lines.

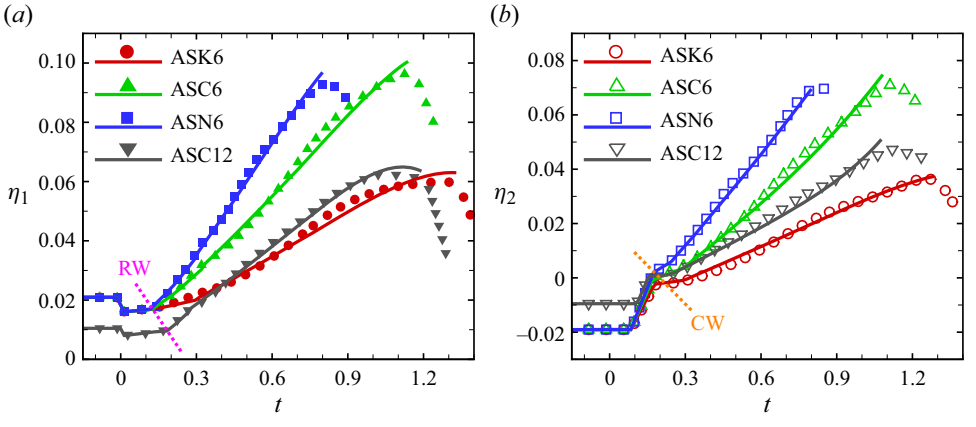

Figure 5. Temporal variations of the amplitudes of the outer (η_1) and inner (η_2) interfaces for the AP cases. The simulation data are marked by symbols and the model results are denoted by lines.

As shown in figure 4, the present model (2.23) well captures the perturbation growths of the IP cases with three fluid layers before reshock, which proves the rationality and validity of the model. Note that the present model based on the linear stability analysis is primarily applicable to the linear stage of the perturbation growth. Previous studies (Ding *et al.* 2019; Sun *et al.* 2020) have demonstrated that the nonlinear effect of the perturbation growth of a shock-accelerated cylindrical fluid layer becomes significant after the collision of reshock on the interface. Therefore, the end time of the present model is chosen as the moment when the reshock meets the perturbed inner interface. It is obvious that the η_1 of the three layers in the IP cases with $n = 6$ almost collapses together until the RW passes through II_1. After the RW collides with II_1, η_1 has almost the same growth in the ASK6 and ASC6 layers that have different $A_{T,2}$. In the ASN6 layer in which $A_{T,2}$ is smallest, η_1 grows more slowly than that in the ASK6 and ASC6 layers. Moreover, the growth rate of η_2 after the impact of TS_1 on II_2 decreases from positive to negative with decreasing $A_{T,2}$. As a result, η_2 in the IP cases changes from increasing to decreasing with time with decreasing $A_{T,2}$ before reshock.

It is shown in figure 5 that the model (2.23) is also verified to show excellent consistency with the DNS results of the perturbation growths of the AP cases with various Atwood

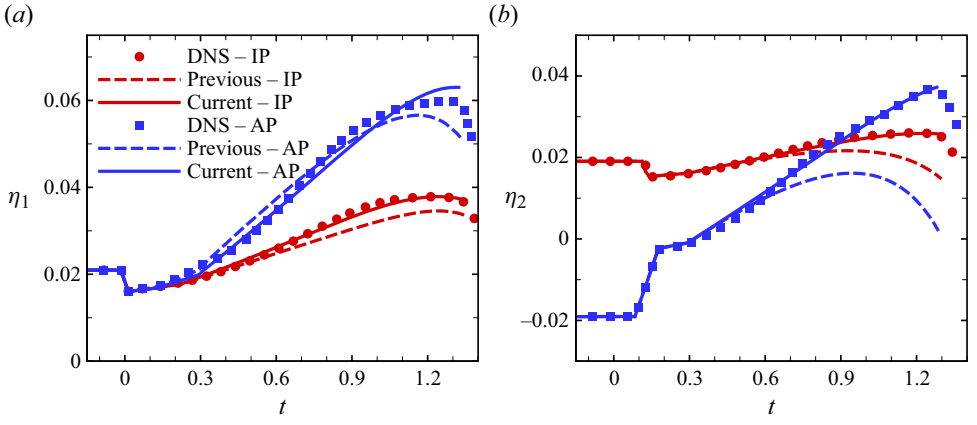

Figure 6. Temporal variations of the amplitudes at the outer (η_1) and inner (η_2) interfaces of the ASK layer with $A_{T,1} = 0.706$ and $A_{T,2} = -0.375$ for the IP and AP cases before reshock. The simulation data are marked by symbols. The results calculated by the previous model (Yuan *et al.* 2023) and the current one are marked by the solid and dashed lines, respectively.

numbers and wavenumbers. The effect of $A_{T,2}$ on the perturbation growths in the AP cases is different from that in the IP cases. Specifically, the growth rates of η_1 after the RW passes through II_1 and of η_2 after TS_1 collides with II_2 increase with decreasing $A_{T,2}$. Consequently, η_1 and η_2 in the AP cases have a faster growth as $A_{T,2}$ decreases before reshock. Moreover, figure 6 is plotted to show the difference between the previous model (Yuan *et al.* 2023) and the current one in predicting the perturbation growth of the ASK layer with $A_{T,1} = 0.706$ and $A_{T,2} = -0.375$. It is evident that the previous model deviates from the DNS results and, thus, is inadequate when $|A_{T,i}| \neq 1$. In contrast, the present model exhibits a much better agreement with the DNS results. This shows that it is necessary to extend the previous model for the fluid layer in a vacuum to the current one for the cases with arbitrary $A_{T,i}$. The above results of the IP and AP cases also indicate that the Atwood number at the inner interface plays an important role in instability evolution of the shock-accelerated cylindrical fluid layer. To this end, the effect of Atwood number at the inner interface is further investigated in the following subsection.

4.3. *Effect of Atwood number at the inner interface*

To elucidate the underlying mechanisms of the effect of Atwood number at the inner interface, various effects that contribute to the perturbation growth of three IP cases with $n = 6$ are specified via the model (2.23) as plotted in figure 7. It is clearly seen that with the decrease of $A_{T,2}$, the contribution of the RM instability to η_1 weakens after the RW collides with II_1. This is due to the fact that the strength of the RW increases with the decrease of $A_{T,2}$. Specifically, as observed from schlieren images in figure 8(*a*), the collision of IS_0 with II_1 is a standard RM instability in which an unperturbed shock impacts upon a perturbed interface (Richtmyer 1960; Meshkov 1969). Since the strength of IS_0 and $A_{T,1}$ are the same in the three layers, η_1 first suffers the same quick drop at $t = 0$ under the compression effect of IS_0 and then increases due to the RM instability by the vorticity deposited by IS_0 on II_1. However, decreasing $A_{T,2}$ leads to a greater density difference at the inner interface and then to a stronger RW. The stronger RW impinging on II_1 results in a stronger RM instability. Figure 8(*c*) shows that the RW has the same phase

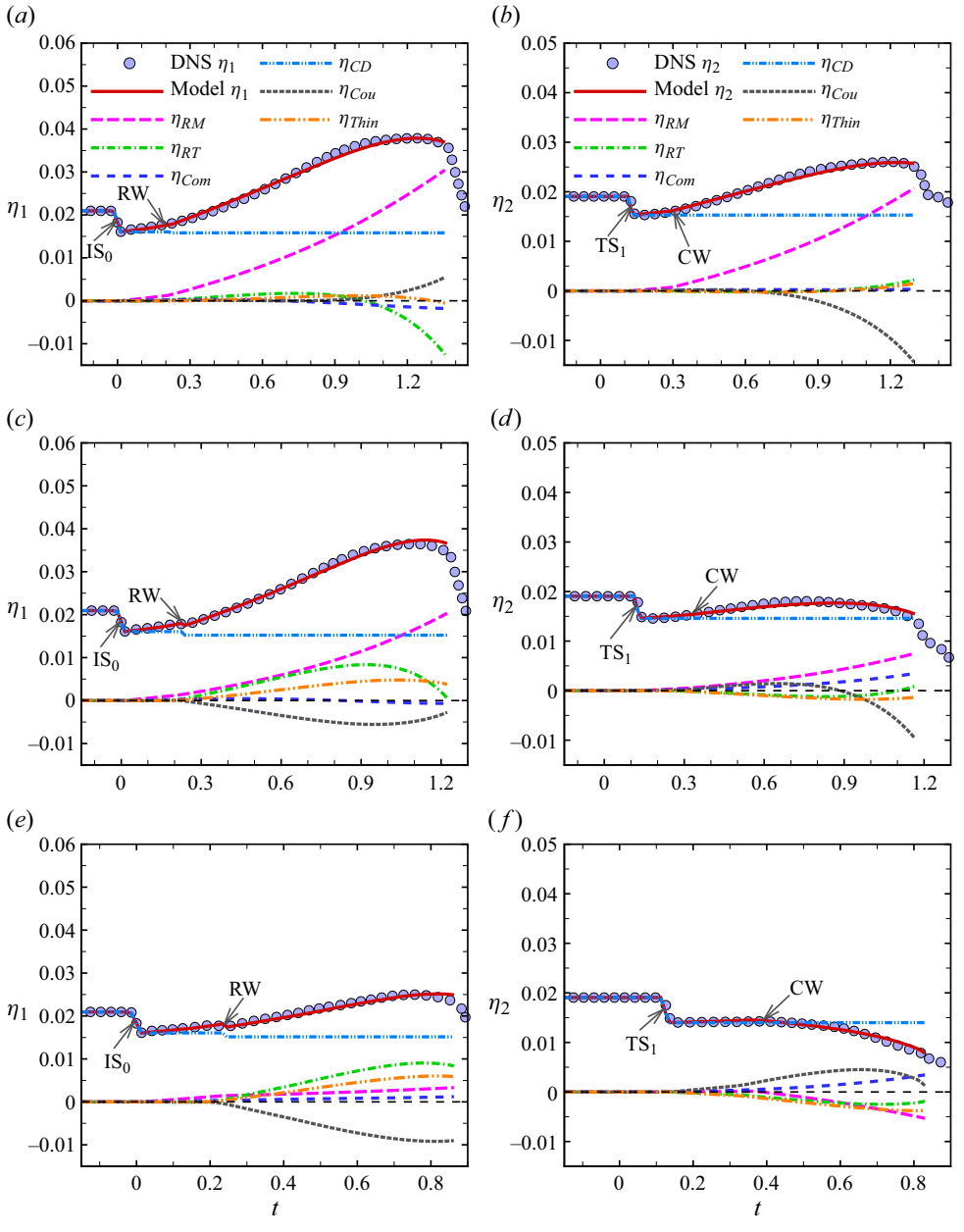

Figure 7. Temporal variations of total amplitudes along with their decomposed contribution terms of the outer (η_1) and inner (η_2) interfaces for the IP cases with (*a*,*b*) ASK layer, (*c*,*d*) ASC layer and (*e*,*f*) ASN layer. The simulation data are marked by symbols and the model results are denoted by lines.

as II_1 and a greater amplitude than II_1. Therefore, the RW first encounters the crest of II_1 whose inward radial velocity is accelerated to a greater value than the trough. This radial velocity difference produces a quick drop in η_1 at $t \approx 0.25$. As $A_{T,2}$ decreases, this drop is increasingly prominent due to the increasing strength of the RW. Note that the RW deposits vorticity on II_1 opposite to the IS_0. Consequently, with decreasing $A_{T,2}$ and an increasing strength of the RW, the greater cancellation on the original vorticity results in the fact that

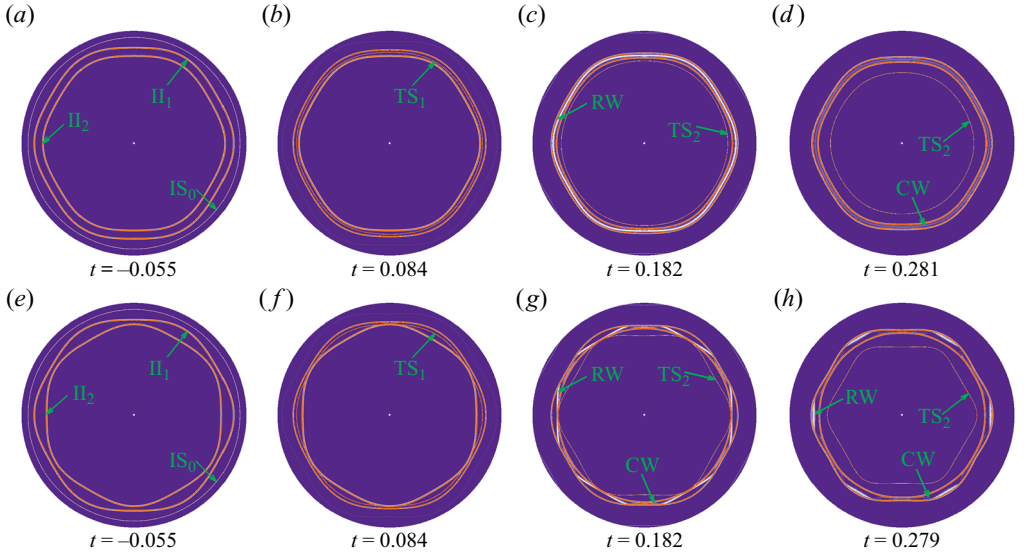

Figure 8. Schlieren images showing the development of wave patterns and interfacial morphologies visualized by the $|\nabla\rho|$ contours for the ASC layer with $n = 6$. The top rows (*a–d*) represent the IP case and the bottom rows (*e–h*) denote the AP case.

the contribution of the RM instability to η_1 weakens after the passage of the RW. For the contribution of the RT effect to η_1, the RW accelerates the inward movement of II_1 and the II_1 is RT unstable. Therefore, after the RW impinges on II_1, the η_{RT} has a positive value that is more significant with the decrease of $A_{T,2}$ shown in figure 7(*a*,*c*,*e*). Moreover, the contributions of the thin-shell correction and the interface coupling effect, especially in the ASN layer, are gradually significant after the RW accelerates II_1 inwards. This is attributed to the fact that the terms of η_{Thin} and η_{Cou} are sensitive to the acceleration of the interface. When $A_{T,2}$ decreases, the interfacial acceleration of II_1 increases, thus leading to the increasing contributions of η_{Thin} and η_{Cou}. In addition, the compressibility effect is not significant for η_1 of the IP cases under the present incident shock strength. The compression/decompression effect contributes to η_1 only when the waves pass through II_1. The above analysis about various contributions to η_1 shows that the decrease of $A_{T,2}$ and enhancement of the RW weaken the contribution of the RM instability, thus, the η_1 of the ASN layer grows slower than that of the ASK and ASC layers.

It is expected that with decreasing $A_{T,2}$, the strength of the CW generated by the collision of the RW with II_1 increases, which has an influence on the growth of η_2. As depicted in figure 7, the growth of η_2 mainly relies on the RM instability whose contribution to η_2 decreases from positive to negative with decreasing $A_{T,2}$. It is clearly seen in figure 8(*b*) that TS_1 has the same phase as II_2 and a smaller amplitude than II_2. As a result, the TS_1 colliding with II_2 leads to a sudden decrease of η_2 at $t \approx 0.12$, and introduces an IP perturbation growth rate at η_2 under the domination of the cylindrical BP effect (Yuan *et al.* 2023). The η_{RM} has a slight increase with time until the CW collides with II_2. As depicted in figure 8(*d*), the CW has the same phase as II_2 and deposits vorticity on II_2 by baroclinic processes to affect the growth of η_{RM}. With decreasing $A_{T,2}$ and an increasing strength of the CW, the contribution of the RM instability to η_2 after the passage of the CW decreases from positive to negative. The RT effect is also influenced by the $A_{T,2}$.

Since the stronger CW leads to greater inward acceleration at the heavy/light interface II_2, the RT-stable II_2 has a more significant negative contribution from the RT effect as $A_{T,2}$ decreases. Furthermore, as the strength of the CW increases, the contribution of the thin-shell correction η_{Thin}, sensitive to the acceleration of II_2, decreases from positive in the ASK layer to negative in the ASN layer, and the contribution of the interface coupling effect η_{Cou}, also sensitive to the acceleration of II_2, increases from negative in the ASK layer to positive in the ASN layer. Additionally, the inner fluid of II_2 is lighter and more increasingly compressible as $A_{T,2}$ decreases and, thus, the compressibility effect η_{Com} has an increasing contribution to promote the growth of η_2. The above analysis indicates the decrease of $A_{T,2}$ and enhancement of the CW significantly affect various contributions to the growth of η_2 in the IP cases, and the decreasing contribution of the RM instability mainly determining the growth of η_2 results in the change of the growth of η_2 from increasing to decreasing with time.

The effect of the Atwood number at the inner interface on the instability evolutions in the AP cases is also investigated. Figure 9 shows various contributions to the perturbation growths of the outer and inner interfaces. For the outer interface in the AP cases, the contribution of the RM instability is enhanced by decreasing $A_{T,2}$, which is different from the diminished RM contribution in the IP cases. This is due to the fact that the AP collision between TS_1 and II_2 causes the AP impact of the generated RW with II_1 as shown in figure 8(*f*,*g*). On the one hand, the RW firstly impacts upon the trough of II_1 that consequently obtains a greater inward radial velocity than the crest. This radial velocity difference produces the quick increase of η_1 at $t \approx 0.2$, which is the decompression effect of the RW. The strength of the RW increases with decreasing $A_{T,2}$ and, thus, the decompression effect of the RW is more significant at lower $A_{T,2}$, as shown in figure 9(*c*,*e*). On the other hand, the RW produces vorticity deposition with the same direction as the vorticity deposited by the initial IS_0 on II_1. With decreasing $A_{T,2}$ and an increasing strength of the RW, more vorticity is deposited on II_1 and the contribution of the RM instability η_{RM} is enhanced. Sharing the same base flow with the IP cases, the AP cases have the same time-varying trends of η_{RT} and η_{Thin} as the corresponding IP cases. Note that the interface coupling effect depends on not only the motion of the interface itself but also the perturbation at another interface. These complex factors make η_{Cou} always decrease to suppress the growth of η_1 for the AP cases and the negative contribution of η_{Cou} is enhanced with decreasing $A_{T,2}$. Additionally, the compressibility effect η_{Com} always has a negative contribution to the growth of η_1 and is less affected by $A_{T,2}$. According to the effect of $A_{T,2}$ to various contributions, the reason for increasing growth of η_1 with decreasing $A_{T,2}$ is that the main contribution to η_1 is the enhanced RM instability as $A_{T,2}$ decreases.

For the inner interface of the AP cases, due to the compression effect of TS_1, η_2 increases quickly to 0 at $t \approx 0.12$ and then grows towards the opposite direction compared with its initial phase. This phenomenon, induced by the vorticity deposited by TS_1 on II_2, is known as phase reversal (Brouillette 2002). This phase reversal is followed by collision of the CW with II_2. As shown in figure 8(*g*), the CW reflecting from the trough of II_1 collides with II_2 whose corresponding part is accelerated to move inwards while the rest of II_2 still keeps its original radial velocity. Thus, this radial velocity difference leads to a slight AP growth rate of η_2 at $t \approx 0.25$. Besides, the CW also deposits vorticity with the same direction as the vorticity deposited by TS_1 on II_2. With decreasing $A_{T,2}$ and an increasing strength of the CW, more vorticity is produced on II_2 and, thus, the

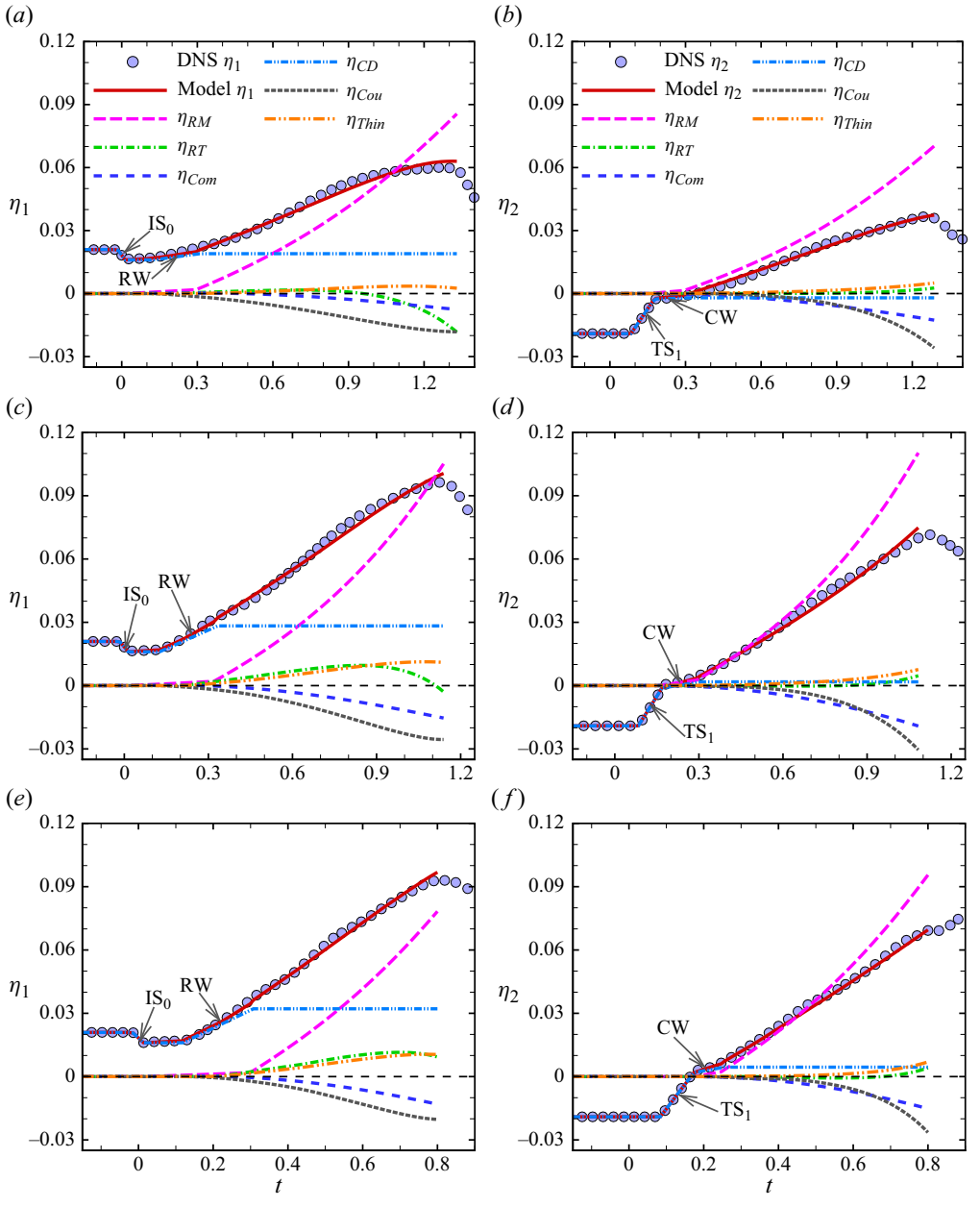

Figure 9. Temporal variations of total amplitudes along with their decomposed contribution terms of the outer (η_1) and inner (η_2) interfaces for the AP cases with (*a*,*b*) the ASK layer, (*c*,*d*) the ASC layer and (*e*,*f*) the ASN layer. The simulation data are marked by symbols and the model results are denoted by lines.

RM instability has a stronger contribution to η_2. Moreover, the contributions of the RT effect and thin-shell correction can be neglected and are less affected by $A_{T,2}$, as shown in figure 9(*b*,*d*,*f*). The interface coupling effect has a negative contribution to the growth of η_2 and is enhanced by decreasing $A_{T,2}$. Like the growth of the outer interface, the faster growth of the inner interface in the AP cases with decreasing $A_{T,2}$ is caused by the stronger RM instability.

5. Concluding remarks

Instability evolution of a shock-accelerated cylindrical fluid layer with two interfaces separating three arbitrary-density fluids is theoretically and numerically investigated. A novel model to describe the instability evolution of a shock-accelerated cylindrical fluid layer with arbitrary Atwood numbers is established. Specifically, a linear stability analysis for the incompressible fluid layer is employed to obtain the contributions, including RM instability, RT effect, thin-shell correction and interface coupling effect at two interfaces with arbitrary Atwood numbers. Then the compressibility effect and compression/decompression effects of waves reverberated inside the fluid layer are linearly superimposed on the incompressible model, which makes the novel model able to predict the instability evolution of a shock-accelerated cylindrical fluid layer with arbitrary Atwood numbers. The present model's validity has been established by comparing its results with the DNS of three different fluid-layer configurations. In these configurations the outer and intermediate fluids remain fixed (i.e. $A_{T,1}$ is fixed) and the density of the inner fluid is reduced. The results demonstrate that the model effectively captures the temporal evolutions of the perturbation amplitudes.

The influence of the Atwood number at the inner interface on the instability evolution of the shock-accelerated cylindrical fluid layer has also been examined. In IP cases where the initial IP perturbations are applied to the inner and outer interfaces, it has been observed that the growth rate of η_1 decreases with decreasing $A_{T,2}$. Additionally, the growth of η_2 exhibits a transition from increasing to decreasing with time as $A_{T,2}$ decreases. For AP cases with initial AP perturbations at the inner and outer interfaces, both the increasing growths of η_1 and η_2 with time are enhanced with decreasing $A_{T,2}$. By utilizing the model to analyse the effect of $A_{T,2}$ on each contribution to the instability evolution, it has been discovered that the dominant contribution from the RM instability is greatly influenced by $A_{T,2}$, resulting in the above observations. As $A_{T,2}$ decreases, the density difference at the inner interface increases. This increased density difference leads to the stronger waves reverberated inside the layer, i.e. the CW and RW. The stronger RW and CW produce more vorticity deposition in the opposite direction compared with the vorticity deposited by the incident shock on II_1 and II_2 in the IP cases, and more vorticity deposition in the same direction as the vorticity deposited by the incident shock on II_1 and II_2 in the AP cases. Consequently, as $A_{T,2}$ decreases, the increasing perturbation growth with time is weakened in the IP cases and enhanced in the AP cases.

The current model is capable of describing the instability evolution of a shock-accelerated cylindrical fluid layer with arbitrary Atwood numbers. In the future, the model can be employed to reveal the underlying mechanism behind more parametric effects on the instability evolutions of shock-accelerated cylindrical fluid layers. Moreover, the present model still relies on the numerical or experimental data to obtain the post-wave growth rate of the perturbation. Quantifying the relationship between the post-wave perturbation growth rate and the intensity of each type of wave based on numerical simulations or experiments to further improve the present model would be an intriguing and worthwhile topic for future investigation.

Acknowledgements. The authors are very grateful to Dr Y.-S. Zhang at the Institute of Applied Physics and Computational Mathematics for useful discussions on the algorithm and code.

Funding. This work was supported by the National Natural Science Foundation of China (Nos. 12202436, 12388101, 92052301, 12272371, 92252202, 12293000 and 12293002), by Science Challenge Project, by LCP Fund for Young Scholar (No. 6142A05QN22002) and by the Strategic Priority Research Program of the Chinese Academy of Sciences (No. XDB0500301).

Layer	Interface	Type	$A_{T,i}$	c_i	ΔV_1	ΔV_2	ΔV_r
SAK	II_1	SF_6/air	−0.688	−0.347	−0.296	0.059	0.201
	II_2	air/Kr	0.464	−0.367	−0.208	−0.020	0.232
SKA	II_1	SF_6/Kr	−0.343	−0.436	−0.230	−0.062	0.173
	II_2	Kr/air	−0.469	−0.525	−0.312	0.007	0.205

Table 5. Detailed parameters corresponding to the base flow of SAK and SKA layers with $\alpha_0 = 1.111$. Notations can be found in table 2.

Layer	Interface	Type	a_1/λ_1	a_2/λ_2	n	t_1^-	t_1^+	$\dot{\eta}_{i,t_1^+}$	t_2^-	t_2^+	$\dot{\eta}_{i,t_2^+}$
SAK	II_1	SF_6/air	0.02	0.02	6	−0.022	0.040	0	0.109	0.166	0.013
	II_2	air/Kr	0.02	0.02	6	0.048	0.109	−0.008	—	0.248	−0.004
SKA	II_1	SF_6/Kr	0.02	0.02	6	−0.021	0.042	0	0.168	0.229	0.011
	II_2	Kr/air	0.02	0.02	6	0.092	0.146	0.002	—	0.302	0.018

Table 6. Detailed parameters corresponding to perturbed SAK and SKA layers. Notations can be found in table 3.

Declaration of interests. The authors report no conflict of interest.

Author ORCIDs.
Ming Yuan https://orcid.org/0000-0002-2602-9990;
Zhiye Zhao https://orcid.org/0000-0003-1509-5084;
Luoqin Liu https://orcid.org/0000-0002-6020-3702;
Nan-Sheng Liu https://orcid.org/0000-0001-9128-1933;
Xi-Yun Lu https://orcid.org/0000-0002-0737-6460.

Appendix. Further validation of the present model

It has been verified in § 4 that the current model (2.23) is capable of accurately describing the perturbation growth of a shock-accelerated cylindrical fluid layer with a fixed outer interface characterized by a light/heavy configuration. To further validate that the current model is suitable for layers with arbitrary configurations (or arbitrary $A_{T,i}$), DNS has also been conducted for two cases with the outer interface characterized by a heavy/light configuration. Specifically, these two cases, namely SF_6/air/Kr (SAK) and SF_6/Kr/air (SKA), are characterized by the outer interfaces with the post-shock Atwood numbers of −0.688 and −0.343, respectively. The perturbed interfaces of the layer for these two cases are IP. Detailed parameters for the base flow are listed in table 5 and the parameters for the perturbed SAK and SKA layers are shown in table 6. The remarkable agreement depicted in figure 10 indicates that the present model (2.23) can describe the perturbation growth of a fluid layer with an outer interface characterized by a heavy/light configuration. Moreover, the present model is able to successfully capture the phase inversion of the outer interface as demonstrated in figure 10(*a*,*c*), and accurately describes the various contributions to the perturbation growths at both the outer and inner interfaces.

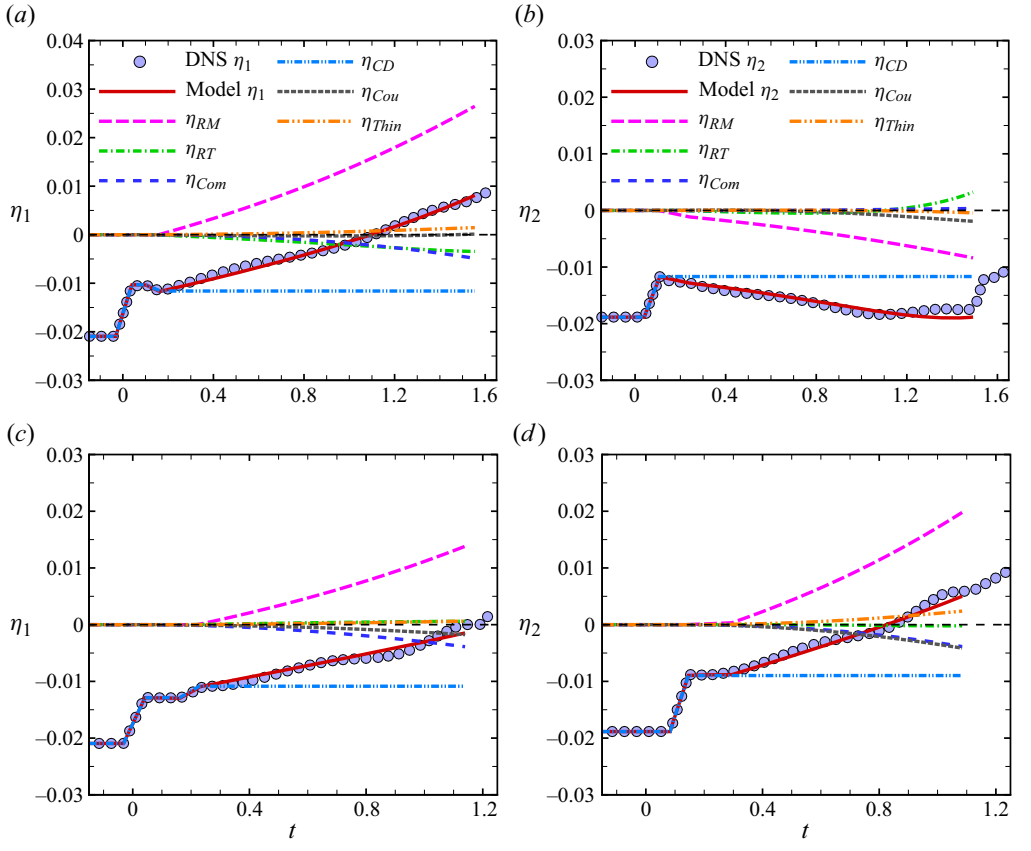

Figure 10. The perturbation amplitudes of the outer (η_1) and inner (η_2) interfaces on the (*a*,*b*) SAK layer, (*c*,*d*) SKA layer along with their decomposed contribution terms versus time for the IP case before reshock. The simulation data marked by symbols are added for comparison.

References

Abarzhi, S.I., Bhowmick, A.K., Naveh, A., Pandian, A., Swisher, N.C., Stellingwerf, R.F. & Arnett, W.D. 2019 Supernova, nuclear synthesis, fluid instabilities, and interfacial mixing. *Proc. Natl Acad. Sci. USA* **116** (37), 18184–18192.

Abu-Shawareb, H., *et al.* 2022 Lawson criterion for ignition exceeded in an inertial fusion experiment. *Phys. Rev. Lett.* **129** (7), 075001.

Amendt, P., Colvin, J.D., Tipton, R.E., Hinkel, D.E., Edwards, M.J., Landen, O.L., Ramshaw, J.D., Suter, L.J., Varnum, W.S. & Watt, R.G. 2002 Indirect-drive noncryogenic double-shell ignition targets for the National Ignition Facility: design and analysis. *Phys. Plasmas* **9** (5), 2221–2233.

Arnett, W.D., Bahcall, J.N., Kirshner, R.P. & Woosley, S.E. 1989 Supernova 1987A. *Annu. Rev. Astron. Astrophys.* **27** (1), 629–700.

Bell, G.I. 1951 Taylor instability on cylinders and spheres in the small amplitude approximation. *Tech. Rep. No.* LA-1321. Los Alamos Scientific Laboratory.

Betti, R. & Hurricane, O.A. 2016 Inertial-confinement fusion with lasers. *Nat. Phys.* **12** (5), 435–448.

Brouillette, M. 2002 The Richtmyer–Meshkov instability. *Annu. Rev. Fluid Mech.* **34** (1), 445–468.

Chen, C., Wang, H., Zhai, Z. & Luo, X. 2023*a* Attenuation of perturbation growth of single-mode SF_6–air interface through reflected rarefaction waves. *J. Fluid Mech.* **969**, R1.

Chen, C., Xing, Y., Wang, H., Zhai, Z. & Luo, X. 2023*b* Freeze-out of perturbation growth of single-mode helium–air interface through reflected shock in Richtmyer–Meshkov flows. *J. Fluid Mech.* **956**, R2.

Chisnell, R.F. 1998 An analytic description of converging shock waves. *J. Fluid Mech.* **354**, 357–375.

DING, J., LI, J., SUN, R., ZHAI, Z. & LUO, X. 2019 Convergent Richtmyer–Meshkov instability of a heavy gas layer with perturbed outer interface. *J. Fluid Mech.* **878**, 277–291.

DING, J., SI, T., YANG, J., LU, X.-Y., ZHAI, Z. & LUO, X. 2017 Measurement of a Richtmyer–Meshkov instability at an air–SF_6 interface in a semiannular shock tube. *Phys. Rev. Lett.* **119** (1), 014501.

EPSTEIN, R. 2004 On the Bell–Plesset effects: the effects of uniform compression and geometrical convergence on the classical Rayleigh–Taylor instability. *Phys. Plasmas* **11** (11), 5114–5124.

FU, C.-Q., ZHAO, Z., XU, X., WANG, P., LIU, N.-S., WAN, Z.-H. & LU, X.-Y. 2022 Nonlinear saturation of bubble evolution in a two-dimensional single-mode stratified compressible Rayleigh–Taylor instability. *Phys. Rev. Fluid* **7** (2), 023902.

GE, J., LI, H., ZHANG, X. & TIAN, B. 2022 Evaluating the stretching/compression effect of Richtmyer–Meshkov instability in convergent geometries. *J. Fluid Mech.* **946**, A18.

HENRY DE FRAHAN, M.T., MOVAHED, P. & JOHNSEN, E. 2015 Numerical simulations of a shock interacting with successive interfaces using the discontinuous Galerkin method: the multilayered Richtmyer–Meshkov and Rayleigh–Taylor instabilities. *Shock Waves* **25**, 329–345.

HESTER, J.J. 2008 The Crab Nebula: an astrophysical chimera. *Annu. Rev. Astron. Astrophys.* **46** (1), 127–155.

JACOBS, J.W., JENKINS, D.G., KLEIN, D.L. & BENJAMIN, R.F. 1995 Nonlinear growth of the shock-accelerated instability of a thin fluid layer. *J. Fluid Mech.* **295**, 23–42.

JACOBS, J.W., KLEIN, D.L., JENKINS, D.G. & BENJAMIN, R.F. 1993 Instability growth patterns of a shock-accelerated thin fluid layer. *Phys. Rev. Lett.* **70** (5), 583–586.

KANE, J., DRAKE, R.P. & REMINGTON, B.A. 1999 An evaluation of the Richtmyer–Meshkov instability in supernova remnant formation. *Astrophys. J.* **511** (1), 335–340.

KISHONY, R. & SHVARTS, D. 2001 Ignition condition and gain prediction for perturbed inertial confinement fusion targets. *Phys. Plasmas* **8** (11), 4925–4936.

LI, J., DING, J., LUO, X. & ZOU, L. 2022 Instability of a heavy gas layer induced by a cylindrical convergent shock. *Phys. Fluids* **34** (4), 042123.

LIANG, Y., LIU, L., ZHAI, Z., SI, T. & WEN, C.-Y. 2020 Evolution of shock-accelerated heavy gas layer. *J. Fluid Mech.* **886**, A7.

LIANG, Y. & LUO, X. 2021 On shock-induced heavy-fluid-layer evolution. *J. Fluid Mech.* **920**, A13.

LIANG, Y. & LUO, X. 2022*a* On shock-induced evolution of a gas layer with two fast/slow interfaces. *J. Fluid Mech.* **939**, A16.

LIANG, Y. & LUO, X. 2022*b* On shock-induced light-fluid-layer evolution. *J. Fluid Mech.* **933**, A10.

LIANG, Y. & LUO, X. 2023 Hydrodynamic instabilities of two successive slow/fast interfaces induced by a weak shock. *J. Fluid Mech.* **955**, A40.

LOMBARDINI, M., PULLIN, D.I. & MEIRON, D.I. 2014 Turbulent mixing driven by spherical implosions. Part 1. Flow description and mixing-layer growth. *J. Fluid Mech.* **748**, 85–112.

LUO, X., LI, M., DING, J., ZHAI, Z. & SI, T. 2019 Nonlinear behaviour of convergent Richtmyer–Meshkov instability. *J. Fluid Mech.* **877**, 130–141.

MESHKOV, E.E. 1969 Instability of the interface of two gases accelerated by a shock wave. *Fluid Dyn.* **4** (5), 101–104.

MIKAELIAN, K.O. 1985 Richtmyer–Meshkov instabilities in stratified fluids. *Phys. Rev.* A **31** (1), 410–419.

MIKAELIAN, K.O. 1990 Rayleigh–Taylor and Richtmyer–Meshkov instabilities and mixing in stratified spherical shells. *Phys. Rev.* A **42** (6), 3400–3420.

MIKAELIAN, K.O. 1995 Rayleigh–Taylor and Richtmyer–Meshkov instabilities in finite-thickness fluid layers. *Phys. Fluids* **7** (4), 888–890.

MIKAELIAN, K.O. 1996 Numerical simulations of Richtmyer–Meshkov instabilities in finite-thickness fluid layers. *Phys. Fluids* **8** (5), 1269–1292.

MIKAELIAN, K.O. 2005 Rayleigh–Taylor and Richtmyer–Meshkov instabilities and mixing in stratified cylindrical shells. *Phys. Fluids* **17** (9), 094105.

PLESSET, M.S. 1954 On the stability of fluid flows with spherical symmetry. *J. Appl. Phys.* **25** (1), 96–98.

RAYLEIGH, LORD 1883 Investigation of the character of the equilibrium of an incompressible heavy fluid of variable density. *Proc. Lond. Math. Soc.* **s1–14** (1), 170–177.

RICHTMYER, R.D. 1960 Taylor instability in shock acceleration of compressible fluids. *Commun. Pure Appl. Maths* **13** (2), 297–319.

SUN, R., DING, J., ZHAI, Z., SI, T. & LUO, X. 2020 Convergent Richtmyer–Meshkov instability of heavy gas layer with perturbed inner surface. *J. Fluid Mech.* **902**, A3.

TAYLOR, G.I. 1950 The instability of liquid surfaces when accelerated in a direction perpendicular to their planes. I. *Proc. R. Soc. Lond.* A **201** (1065), 192–196.

WADAS, M.J., KHIEU, L.H., CEARLEY, G.S., LEFEVRE, H.J., KURANZ, C.C. & JOHNSEN, E. 2023 Saturation of vortex rings ejected from shock-accelerated interfaces. *Phys. Rev. Lett.* **130** (19), 194001.

WALCHLI, B. & THORNBER, B. 2017 Reynolds number effects on the single-mode Richtmyer–Meshkov instability. *Phys. Rev.* E **95** (1), 013104.

WU, J., LIU, H. & XIAO, Z. 2021 Refined modelling of the single-mode cylindrical Richtmyer–Meshkov instability. *J. Fluid Mech.* **908**, A9.

YAN, Z., FU, Y., WANG, L., YU, C. & LI, X. 2022 Effect of chemical reaction on mixing transition and turbulent statistics of cylindrical Richtmyer–Meshkov instability. *J. Fluid Mech.* **941**, A55.

YUAN, M., ZHAO, Z., LIU, L., WANG, P., LIU, N.-S. & LU, X.-Y. 2023 Instability evolution of a shock-accelerated thin heavy fluid layer in cylindrical geometry. *J. Fluid Mech.* **969**, A6.

ZHANG, D., DING, J., SI, T. & LUO, X. 2023 Divergent Richtmyer–Meshkov instability on a heavy gas layer. *J. Fluid Mech.* **959**, A37.

ZHANG, S., LIU, H., KANG, W., XIAO, Z., TAO, J., ZHANG, P., ZHANG, W. & HE, X.-T. 2020 Coupling effects and thin-shell corrections for surface instabilities of cylindrical fluid shells. *Phys. Rev.* E **101** (2), 023108.

ZHAO, Z., WANG, P., LIU, N.-S. & LU, X.-Y. 2020 Analytical model of nonlinear evolution of single-mode Rayleigh–Taylor instability in cylindrical geometry. *J. Fluid Mech.* **900**, A24.

ZHOU, Y., CLARK, T.T., CLARK, D.S., GAIL GLENDINNING, S., AARON SKINNER, M., HUNTINGTON, C.M., HURRICANE, O.A., DIMITS, A.M. & REMINGTON, B.A. 2019 Turbulent mixing and transition criteria of flows induced by hydrodynamic instabilities. *Phys. Plasmas* **26** (8), 080901.

ZHOU, Y., *et al.* 2021 Rayleigh–Taylor and Richtmyer–Meshkov instabilities: a journey through scales. *Physica* D **423**, 132838.

ZOU, L., AL-MAROUF, M., CHENG, W., SAMTANEY, R., DING, J. & LUO, X. 2019 Richtmyer–Meshkov instability of an unperturbed interface subjected to a diffracted convergent shock. *J. Fluid Mech.* **879**, 448–467.